Analyses of Electrochemical Phenomena at Hg Ultramicroelectrodes

by

Tim Zhang

A dissertation submitted in partial fulfillment
of the requirements for the degree of
Doctor of Philosophy
(Chemistry)
in the University of Michigan
2017

Doctoral Committee:

Associate Professor Stephen Maldonado, Chair
Professor Mark Banaszak Holl
Associate Professor Bart Bartlett
Professor Cagliyan Kurdak

timzhang@umich.edu

ORCID iD: 0000-0002-0710-3374

Dedication

For my parents

Acknowledgements

The journey towards a PhD is not an easy one, but I am glad to say that I have received the help and support of many people along the way. I would like to thank Professor Stephen Maldonado for his help, advice, and insight throughout these four years, from which I started out as a student with no electrochemistry knowledge. I would like my committee members, Professor Mark Banaszak Holl, Professor Bart Bartlett and Professor Cagliyan Kurdak, for bringing their perspectives to better my research. I would like to thank Dr. Zheng Zheng, for teaching me how to make the ultramicroelectrodes that were the basis of my PhD. I would like to thank all the members, past and present, of the Maldonado Group, who have developed an atmosphere in lab where everyone is willing to help each other, whether it be through collaboration or simply acting as a sounding board for ideas. I am grateful for such a welcoming environment. And lastly, I would like to thank my parents, for supporting me no matter what and rooting for me for this entire journey.

Table of Contents

List of Figures

Abstract

The focus of this thesis is the use of Hg ultramicroelectrodes (UMEs) as platforms to study electrochemical phenomena related to the electrodeposition of individual semiconductor micro/nano crystals by the electrochemical liquid-liquid-solid (ec-LLS) growth technique. ec-LLS is a non-energy intensive technique capable of producing crystalline semiconductor microwires at ambient conditions. ec-LLS growth to date has been carried out in the form of liquid metal electrode arrays, which results in microwire films with a range of morphologies. Voltammetric and chronoamperometric experiments were performed to investigate the electrodeposition of Ge by ec-LLS, including the associated adsorption and redox steps. The context of this work is to better understand ec-LLS in general by exploiting the advantages offered with small volumes of liquid metals. UMEs allow the opportunity to identify possible correlations between current transient and crystal growth.

This thesis describes the following three primary findings. In Chapter 2, the data implicate that Ge crystal growth by ec-LLS is different at small Hg volumes as compared to bulk Hg pools. Recorded voltammetry with Hg UMEs showed unexpectedly slow introduction of Ge into the liquid metal. Unique morphologies never observed before in any electrodeposition context are detailed. In Chapter 3, the possibility that size affects adsorption of species to Hg interfaces was tested with both macrosize and microsize Hg electrodes. The data argue against any significant influence of electrocapillarity effects but do indicate that mass

transport at small sizes can greatly alter adsorptive voltammetric features in some cases. In Chapter 4, a further assessment of the electrochemical reduction of GeO_2 dissolved in aqueous electrolytes is presented. Voltammetric data for Hg UMEs in dilute aqueous solutions of dissolved GeO_2 showed the rate of Ge introduction into the liquid metal, and the ratio between the anodic and cathodic charge argued for a complex and atom-inefficient process (with respect to introduction of Ge^0 into liquid Hg).

A final chapter is included in this thesis that describes several possible future directions for this work. Three topics are described. First, observations from preliminary attempts to perform Ge ec-LLS at Hg nanodroplets are described. Second, the preparation of UMEs with Ga is shown and discussed in terms of preparation challenges. Third, an alternative UME platform is demonstrated that consists of a single hole patterned in a photoresist film. Opportunities and challenges for this strategy are relayed.

Chapter 1

Introduction

1.1 Background

Semiconductor materials are the key components in technologies such as transistors, batteries, and photovoltaics.[1-4] The prevalent trend in these devices is to become smaller, faster, more powerful and more energy-efficient. Accordingly, methods to synthesize high-quality semiconductors at the microscale and nanoscale are increasing in importance. Materials with physical designs that are long and thin like microwires and nanowires are especially advantageous to several of these technologies since they allow tuning of the optical, electronic, and mechanical properties.[5-8]

There is a variety of synthetic strategies for making one-dimensional semiconductors. Top-down methods, such as etching of bulk wafers, require destructively subtracting material from a larger block to form the microwire and nanowire structures and are thus wasteful in terms of material consumption.[9-12] Bottom-up methods, such as nucleating and growing one-dimensional crystals directly as microwires and nanowires, are intrinsically more atom efficient and can potentially lower synthesis costs.[3,4,9,13] The primary disadvantage of bottom-up synthetic methods is that knowledge of the crystal growth process is necessary to avoid incorporation of defects and impurities, and produce high quality materials.[14]

Two of the most actively explored methods of nanowire synthesis are vapor-liquid-solid growth (VLS) [15-17] and solution-liquid-solid growth (SLS).[18-20] In the VLS technique, shown in

Figure 1.1, a metal particle is heated in an environment containing a gaseous precursor. In the SLS method, shown in Figure 1.2, a metal particle is suspended in hot liquid solvent with a dissolved precursor. In both, the high temperature melts the metal particle and facilitates precursor decomposition into it. Continual dissolution of the decomposed precursor leads to saturation of the liquid metal solution, followed by nucleation and one dimensional crystal growth. The relative rates of dissolution, nucleation, and crystallization depend strongly on the parameters and materials used for these processes. In particular, the size of the metal particle strongly dictates the diameter of the growing wire.[15,21] The choice of the metal particle is important and limited by phase equilibria, as it must be able to form an alloy, ideally an eutectic compound, with the precursor.[15,21] There is also the possibility of incorporation of the metal as an impurity into the semiconductor.[21,22] Despite their superficial similarities, VLS and SLS are limited in separate ways. VLS methods primarily require a considerable amount of auxiliary equipment to control the temperature, pressures, and flow rate of gaseous species.[23,24] In addition, typically high (>>>25°C) temperatures are required, that limit the potential options for supporting substrates.[25,26] SLS methods can be performed with considerably simpler apparatus but are difficult to control with respect to the rates of precursor decomposition, dissolution, and nucleation/crystallization, and typically require exotic solvents.[27,28] Furthermore, SLS most naturally occurs with suspended particles and is not easily adapted to yield high densities of uniform nanowires.[21,29]

1.2 Electrochemical Liquid-Liquid-Solid Growth

In our group, we have developed an electrochemical counterpart that has strong similarities to VLS and SLS. The electrochemical liquid-liquid solid (ec-LLS) process makes use

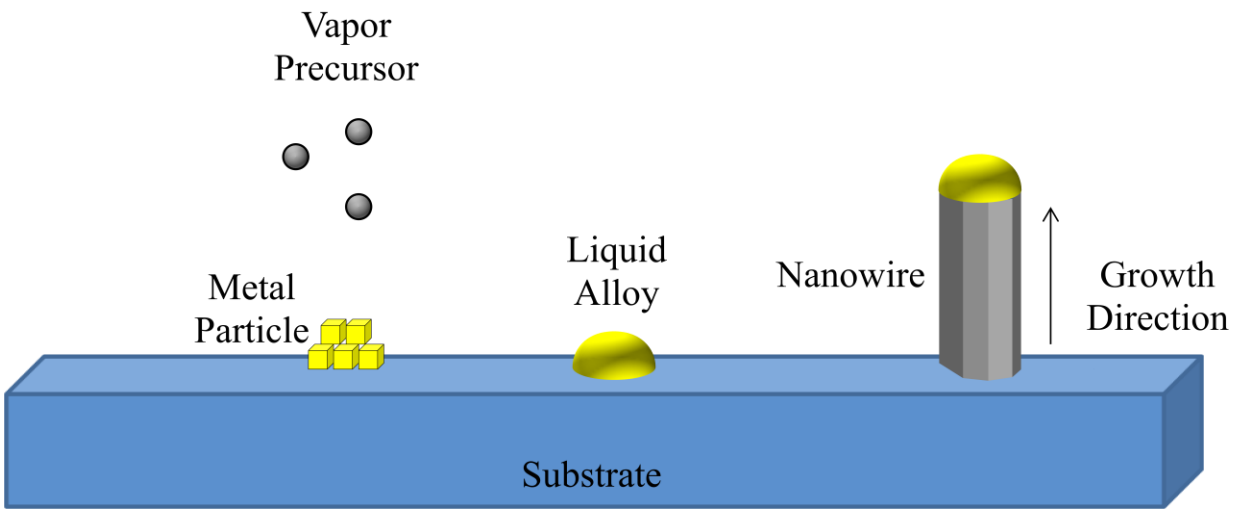

Figure 1.1 Schematic depiction of the vapor-liquid-solid growth process. The metal particle on the substrate is heated in a vacuum environment with a vapor precursor (left) to form a liquid alloy (middle). Continuous dissolution of the precursor into the alloy leads to saturation, nucleation and one-dimensional crystal growth (right).

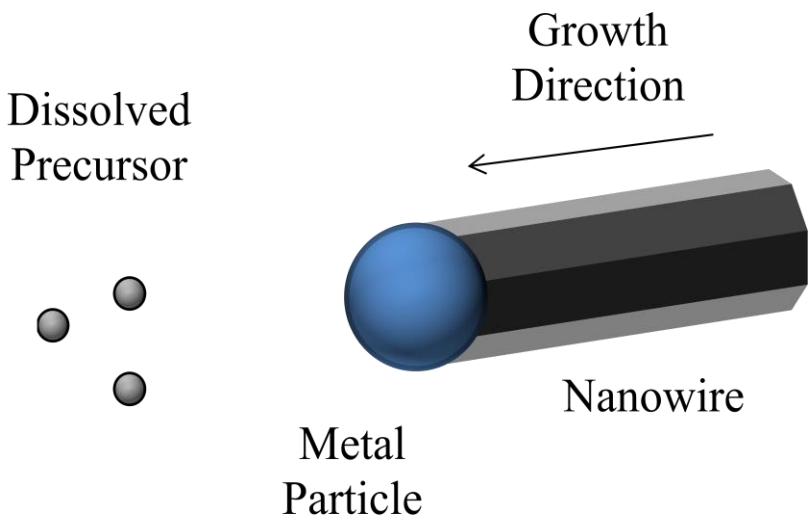

Figure 1.2 Schematic depiction of the solution-liquid-solid growth process. The metal particle and dissolved precursor are in an organic solvent solution, which is heated to form a liquid alloy between the particle and precursor. Continuous dissolution of the precursor into the alloy leads to saturation, nucleation and one-dimensional crystal growth.

of liquid metal not only as the crystal growth medium but also as the working electrode in an electrochemical cell, as shown in Figure 1.3. In ec-LLS, the decomposition of precursors is controlled electrochemically, allowing precision over start and stop times as well as the rates of dissolution into the liquid metal. Importantly, ec-LLS can be performed under ambient conditions, even in aqueous solutions. As the liquid metal must be in contact with a current collector, ec-LLS opens up the option of growth of nanowires on conductive substrates. ec-LLS has been used to grow several crystalline semiconductors including Ge, Si, GaAs, InAs, and GaSb.[30-40]

To date, much of our group's work on ec-LLS has been done in one of two ways: (*1*) with bulk pools of liquid metal electrodes or (*2*) with arrays of liquid metal micro- /nanodroplets. While both tactics have been advantageous for different purposes, each limits a more comprehensive understanding of the ec-LLS process. Specifically, although current-time or current-potential data are always collected during ec-LLS, the use of bulk liquid metal pools or arrays of many liquid metal droplets complicates their analysis and any possible correlations that would shed insight on the crystal formation process.

1.3 Ultramicroelectrodes

In contrast, performing ec-LLS with an ultramicroelectrode is desirable for fundamental study. Ultramicroelectrodes are defined as electrodes in which the electrode diameter is between the range of tens of micrometers to 100 angstroms.[41] The small electrode area of the ultramicroelectrode is suitable for electrodepositing a single liquid metal droplet. If the dimensions are small enough, ec-LLS could be performed to produce only a single microwire. The current recorded with an ultramicroelectrode would then necessarily describe the growth

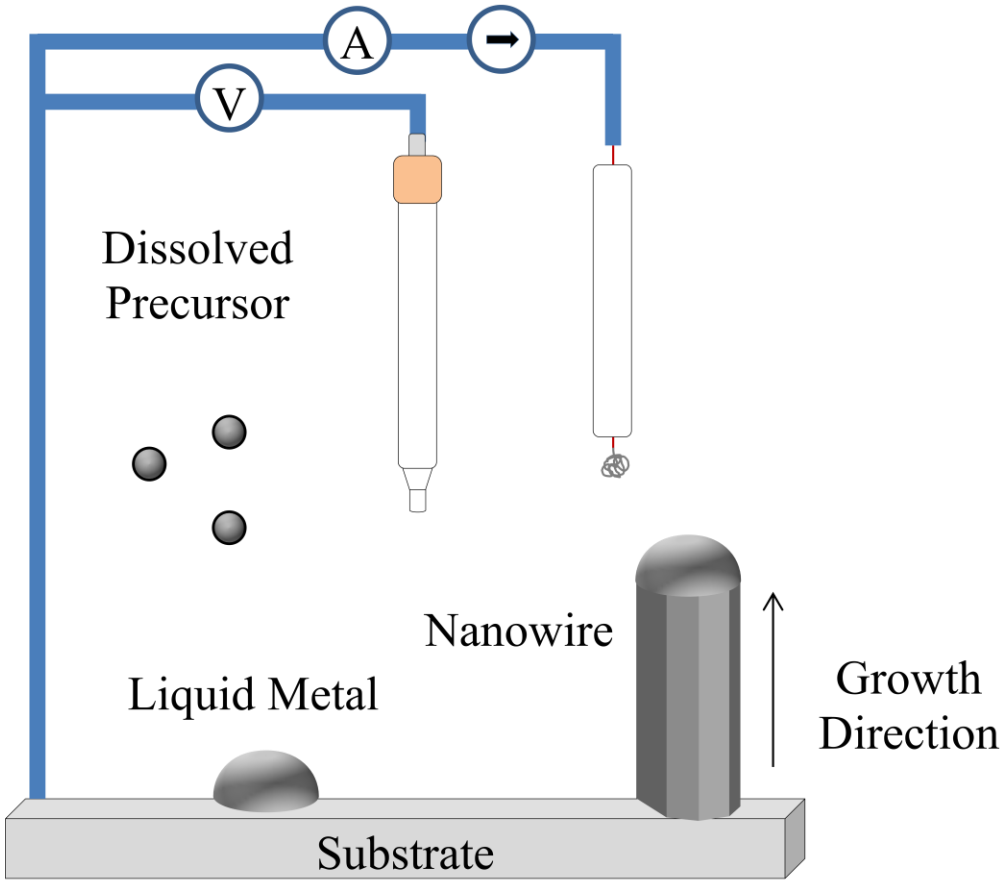

Figure 1.3 Schematic depiction of the electrochemical liquid-liquid-solid growth method. The liquid metal on the substrate is immersed in a solution containing a dissolved precursor. An electric bias is applied to reduce the precursor, which then dissolves into the liquid metal to form an alloy. Continuous dissolution of the precursor into the alloy leads to saturation, nucleation and one-dimensional crystal growth.

process of a single microwire or single crystal. Additionally, the small (nanoamp) currents minimize ohmic drop distortions, increasing the quality of the raw data and enabling the use of less conductive electrolytes, such as low concentration solutions or non-aqueous media. Ultramicroelectrodes also feature precisely defined mass transport through radial diffusion which dominates at long times. The known mass transport rates mean that the ec-LLS process could be studied under kinetic or transport limited conditions. Additionally, the double layer of an ultramicroelectrode is smaller, and the time it takes to charge the capacitance of this layer is proportional the electrode size.[42-44] Therefore, the initial stages of the nucleation and growth process can be studied at much shorter times than are available with a bulk liquid pool electrode.

1.4 Thesis Overview

In this thesis, the underlying premise explored is that individual Hg ultramicroelectrodes are useful probes for studying ec-LLS and phenomena that could be relevant to ec-LLS at small liquid metal droplets. Chapter 2 focuses on Ge ec-LLS at a Hg ultramicroelectrode. Hg was electrodeposited onto a Pt ultramicroelectrode. Its stability was shown by the greater overpotential needed for hydrogen evolution over multiple cycles, and the sigmoidal shape of the cyclic voltammogram in a solution of $Ru(NH_3)_6Cl_3$. Cyclic voltammetry of the Hg ultramicroelectrode in a solution of dissolved GeO_2 at different scan rates showed that Ge does not immediately dissolve into the Hg liquid metal, and that the cathodic charge is much greater than the corresponding anodic charge. The reduction of GeO_2 into Hg is a more complicated process than expected. Chronoamperometry in the same dissolved GeO_2 solution resulted in the formation of a complete Ge crust or an extrusion that sometimes resulted in a coiled microwire

morphology. Ge ec-LLS at Hg microdroplet ultramicroelectrodes also resulted in materials with morphologies that have never been observed before in any electrodeposition context.

Chapter 3 focuses on the absorption and desorption of several ionic species at a Hg microdroplet ultramicroelectrode. The action of surface tension forces on a Hg electrode is potentially more significant on the microscale than the bulk. This premise was tested through analysis of the voltammetric signatures of species that are known to adsorb on Hg interfaces. Cyclic voltammograms over a range of scan rates were taken of bulk Hg pools and Hg ultramicroelectrodes in solutions containing halide anions, heptyl viologen cations, and tetraborate anions. The data was analyzed to determine if surface-based processes are a function of Hg electrode size (volume) and whether this would likely be relevant in ec-LLS performed with small liquid metal droplets.

Chapter 4 focuses on Ge growth in Hg ultramicroelectrodes through varying the GeO_2 concentration in solution. The rate of Ge introduction in to the liquid metal is slower than expected, and reactions other than the reduction of GeO_2 contributed to the cathodic charge observed. The anodic peak associated with the oxidation of zero valent Ge dissolved in the liquid metal does not appear at low concentrations of GeO_2. The anodic peak does not appear immediately, and takes several cycles to emerge and reach a stationary value. The implications of these voltammetric features on the Ge ec-LLS process are discussed.

Chapter 5 focuses on related avenues of research to the previous three chapters that were attempted to expand upon the concepts studied with ec-LLS at Hg microdroplet ultramicroelectrodes. Observations on Ge ec-LLS at Hg nanodroplets, the fabrication of Ga ultramicroelectrodes, and the development of a pinhole photoresist ultramicroelectrode platform are presented in addition to suggestions for future directions.

1.5 References

1. T. J. Kempa, R. W. Day, S.-K. Kim, H.-G. Park and C. M. Lieber, *Energy Environ. Sci.*, **6**, 719 (2013).
2. A. I. Hochbaum and P. Yang, *Chem. Rev.*, **110**, 527 (2010).
3. L. Wei and M. L. Charles, *J. Phys. D: Appl. Phys.*, **39**, R387 (2006).
4. N. P. Dasgupta, J. Sun, C. Liu, S. Brittman, S. C. Andrews, J. Lim, H. Gao, R. Yan and P. Yang, *Adv. Mater.*, **26**, 2137 (2014).
5. C. M. Lieber, *MRS Bull.*, **28**, 486 (2003).
6. Z. He, J. Jie, W. Zhang, W. Zhang, L. Luo, X. Fan, G. Yuan, I. Bello and S.-T. Lee, *Small*, **5**, 345 (2009).
7. J. Greil, A. Lugstein, C. Zeiner, G. Strasser and E. Bertagnolli, *Nano Lett.*, **12**, 6230 (2012).
8. T. J. Athauda, P. Hari and R. R. Ozer, *ACS Appl. Mater. Interfaces*, **5**, 6237 (2013).
9. R. G. Hobbs, N. Petkov and J. D. Holmes, *Chem. Mater.*, **24**, 1975 (2012).
10. Y. Sun, R. A. Graff, M. S. Strano and J. A. Rogers, *Small*, **1**, 1052 (2005).
11. L. Chen, W. Lu and C. M. Lieber, in *Semiconductor Nanowires: From Next-Generation Electronics to Sustainable Energy*, p. 1, The Royal Society of Chemistry (2015).
12. S. Barth, F. Hernandez-Ramirez, J. D. Holmes and A. Romano-Rodriguez, *Prog. Mater Sci*, **55**, 563 (2010).
13. D. Lincot, *Thin Solid Films*, **487**, 40 (2005).
14. M. Law, J. Goldberger and P. Yang, *Annu. Rev. Mater. Res.*, **34**, 83 (2004).
15. R. S. Wagner and W. C. Ellis, *Appl. Phys. Lett.*, **4**, 89 (1964).
16. B. A. Wacaser, K. A. Dick, J. Johansson, M. T. Borgström, K. Deppert and L. Samuelson, *Adv. Mater.*, **21**, 153 (2009).
17. Y. Wu and P. Yang, *J. Am. Chem. Soc.*, **123**, 3165 (2001).
18. T. J. Trentler, K. M. Hickman, S. C. Goel, A. M. Viano, P. C. Gibbons and W. E. Buhro, *Science*, **270**, 1791 (1995).
19. F. Wang, A. Dong, J. Sun, R. Tang, H. Yu and W. E. Buhro, *Inorg. Chem.*, **45**, 7511 (2006).
20. X. Lu, D. D. Fanfair, K. P. Johnston and B. A. Korgel, *J. Am. Chem. Soc.*, **127**, 15718 (2005).
21. F. Wang, A. Dong and W. E. Buhro, *Chem. Rev.*, **116**, 10888 (2016).
22. W. Chen, L. Yu, S. Misra, Z. Fan, P. Pareige, G. Patriarche, S. Bouchoule and P. R. i. Cabarrocas, *Nat. Commun.*, **5**, 4134 (2014).
23. K. W. Kolasinski, *Curr. Opin. Solid State Mater. Sci.*, **10**, 182 (2006).
24. N. Wang, Y. Cai and R. Q. Zhang, *Mater. Sci. Eng., R*, **60**, 1 (2008).
25. B. J. Kim, C. Y. Wen, J. Tersoff, M. C. Reuter, E. A. Stach and F. M. Ross, *Nano Lett.*, **12**, 5867 (2012).
26. M. C. McAlpine, H. Ahmad, D. Wang and J. R. Heath, *Nat Mater*, **6**, 379 (2007).
27. A. T. Heitsch, D. D. Fanfair, H.-Y. Tuan and B. A. Korgel, *J. Am. Chem. Soc.*, **130**, 5436 (2008).
28. A. Dong, H. Yu, F. Wang and W. E. Buhro, *J. Am. Chem. Soc.*, **130**, 5954 (2008).
29. M. Kuno, *Phys. Chem. Chem. Phys.*, **10**, 620 (2008).

30. A. I. Carim, S. M. Collins, J. M. Foley and S. Maldonado, *J. Am. Chem. Soc.*, **133**, 13292 (2011).
31. J. Gu, S. M. Collins, A. I. Carim, X. Hao, B. M. Bartlett and S. Maldonado, *Nano Lett.*, **12**, 4617 (2012).
32. E. Fahrenkrug, J. Gu and S. Maldonado, *J. Am. Chem. Soc.*, **135**, 330 (2013).
33. J. Gu, E. Fahrenkrug and S. Maldonado, *J. Am. Chem. Soc.*, **135**, 1684 (2013).
34. E. Fahrenkrug, J. Gu, S. Jeon, P. A. Veneman, R. S. Goldman and S. Maldonado, *Nano Lett.*, **14**, 847 (2014).
35. L. Ma, J. Gu, E. Fahrenkrug and S. Maldonado, *J. Electrochem. Soc.*, **161**, D3044 (2014).
36. E. Fahrenkrug, J. Gu and S. Maldonado, *Chem. Mater.*, **26**, 4535 (2014).
37. E. Fahrenkrug, J. Biehl and S. Maldonado, *Chem. Mater.*, **27**, 3389 (2015).
38. E. Fahrenkrug and S. Maldonado, *Acc. Chem. Res.*, **48**, 1881 (2015).
39. J. DeMuth, L. Ma, E. Fahrenkrug and S. Maldonado, *Electrochim. Acta*, **197**, 353 (2016).
40. L. Ma, S. Lee, J. DeMuth and S. Maldonado, *RSC Adv.*, **6**, 78818 (2016).
41. I. Rubinstein, *Physical Electrochemistry: Science and Technology*, Taylor & Francis (1995).
42. R. J. Forster, *Chem. Soc. Rev.*, **23**, 289 (1994).
43. J. Heinze, *Angew. Chem., Int. Ed. Engl.*, **32**, 1268 (1993).
44. C. G. Zoski, *Electroanalysis*, **14**, 1041 (2002).

Chapter 2

Electrochemical Liquid-Liquid-Solid Deposition of Ge at Hg Microdroplet Ultramicroelectrodes

2.1 Introduction

To date, a variety of bottom-up methods including vapor-liquid-solid growth,[1-3] solution-liquid-solid growth,[4, 5] and template-defined electrodeposition[6, 7] have been demonstrated for the preparation of crystalline semiconductor micro/nanomaterials.[8, 9] A newly identified method is electrochemical liquid-liquid-solid (ec-LLS) crystal growth, where a liquid metal electrode acts both as the source of electrons for heterogeneous reduction reactions and as the solvent for semiconductor crystal formation.[10, 11] An advantage of ec-LLS over the aforementioned methods is the capacity to produce crystalline semiconductor micro/nanowires in aqueous solution at ambient temperatures and pressures.

The preliminary demonstration of ec-LLS was the electroreduction of dissolved GeO_2 in aqueous solution at bulk Hg pool electrodes.[12] Although the influence of basic ec-LLS parameters (e.g. time, potential, liquid metal type) have since been studied, the size (volume) of Hg electrodes has not yet been directly examined. In contrast to other variables, the Hg pool size

should have influence on both the electrochemical and crystal growth aspects of ec-LLS, as both mass transport to the electrode surface and the ratio of the volume of the growing crystallites to the volume of the liquid metal are increased at microdroplets as compared to bulk liquid pools.

We have previously established that liquid Ga droplets with radii of 10^{-7} m and corresponding volumes of 10^{-15} cm^3 can nucleate single crystalline Ge nano- and microwires.[13,14] There are no previous reports on whether the same is achievable with small Hg droplets, i.e. at volumes 10^{10} times smaller than our previous investigation with Hg as an ec-LLS electrode/medium.[12] The use of Hg microdroplets also presents two additional advantages for study of the ec-LLS process. First, diffusion is fast in such small liquid metal volumes. The diffusivity of Ge in Hg at room temperature has been previously measured as 1.3×10^{-5} cm^2 s^{-1}.[15] With a radius of ~10 μm, any dissolved Ge atom at the electrolyte/Hg interface can diffuse the entire volume of Hg in less than 0.04 s. Thus, there is no meaningful time delay in moving Ge into or out of the Hg microdroplet during the respective electroreduction and electrooxidative experiments that last longer than this time. Second, small Hg microdroplets support small absolute heterogeneous currents, allowing access to undistorted fast scan voltammetry featuring high current densities. This aspect is not true for macroscopic Hg pool electrodes and was a primary reason why the voltammetry has been difficult to study in concentrated (>10 mM) solutions of dissolved GeO_2.[16]

Accordingly, in this report, Hg microdroplet ultramicroelectrodes with radii, *r*, ranging between 5 and 10 μm are prepared through the conversion of platinum (Pt) ultramicroelectrodes by Hg electrodeposition[17] and then used as platforms to attempt Ge ec-LLS. Figure 2.1 summarizes the scheme employed in this work. The presented data explore three primary hypotheses. First, anodic stripping voltammograms indicate an unexpectedly slow rate of

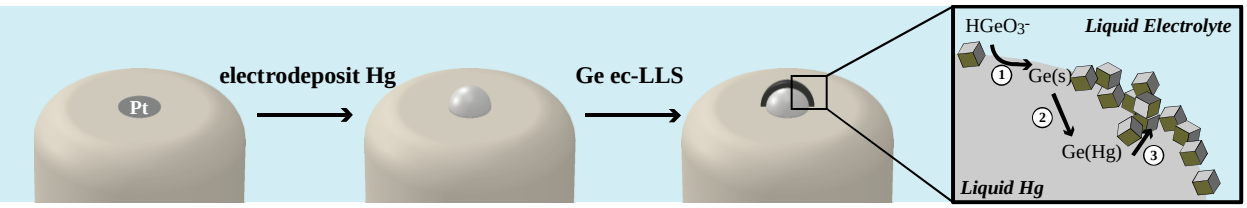

Figure 2.1. Schematic depictions of (left) the formation of an individual Hg microdroplet ultramicroelectrode via the electrodeposition of Hg onto a glass-encased Pt ultramicroelectrode and (right) the elementary steps in Ge ec-LLS at a Hg electrode.

introduction of Ge into Hg through Reaction 1 and a correspondingly small concentration of dissolved Ge in ultra-small volume Hg electrodes.

$$HGeO_3^-(aq) + 4e^- + 2H_2O(l) \rightarrow Ge(s) + 5OH^-(aq) \quad (1)$$

Second, the current transient collected during ec-LLS at a single Hg ultramicroelectrode under a constant applied bias tracks the form of the electrodeposited Ge crystal(s). Third, microdroplet liquid metal electrodes yield unique crystalline Ge morphologies relative to the Ge crystals produced with analogous bulk Hg pool electrodes. A series of voltammetric and amperometric data and scanning electron micrographs are presented that address these topics.

2.2 Experimental

2.2.1 Materials

Pt wire (radius = 12.5 μm, 99.95%) was obtained from Alfa Aesar. $CaCl_2$ (97%, Fluka), C_3H_6O (ACS grade, Fisher), KCl (99%, Sigma-Aldrich), $Ru(NH_3)_6Cl_3$ (98%, Sigma Aldrich), $Hg(NO_3)_2$ (98%, Alfa Aesar), KNO_3 (99%, Acros Organics), HNO_3 (65% Fisher Scientific), Ar(g) (99.998%, Detroit Metro Welding), GeO_2 (99.99%, Sigma-Aldrich), and $Na_2B_4O_7$ (ACS grade, Mallinckrodt) were used as received. Water obtained from a Nanopure II water filtration system with a resistivity > 18 MΩ cm was used throughout.

2.2.2 Ultramicroelectrode Fabrication and Use

Pt wire was glued onto a small piece of glass slide with cyanoacrylate (Bob Smith Industries), and attached to a variable autotransformer with a voltmeter to control the potential applied. The Pt wire was etched under 4 V in a 20 wt% $CaCl_2$, 1:1 (v/v) water-acetone solution for one minute.[18] The etched Pt microwire was then sealed inside a glass capillary tube via heating with a nichrome heating coil.[19] The sealed end was subsequently filed with sandpaper to

expose the Pt wire. Electrical contact to the Pt microwire was made by soldering a copper wire. Scanning electron microscopy was used to determine whether the polishing step exposed a circular microdisk.

Cyclic voltammetry was performed in three electrode cells containing 0.001 M $Ru(NH_3)_6Cl_3$ and 0.1 M KCl to assess ultramicroelectrode behavior. CH Instruments models 420a and 760c potentiostats were used throughout. All reported potentials are referenced to a mercury/mercurous sulfate (E (Hg/Hg_2SO_4)) reference electrode.

Following the protocol of Mauzeroll,[17] a solution containing 0.01 M $Hg(NO_3)_2$, 0.1 M KNO_3, and 0.5% HNO_3 was first prepared, purged with Ar(g) for 15 min to eliminate oxygen from the solution, and then kept under an Ar(g) blanket. Hg was then electrodeposited onto the Pt ultramicroelectrode immersed in this solution while biased at -0.1 V for 5 min. The Hg-capped ultramicroelectrode was then transferred to another electrochemical cell containing an Ar(g)-purged solution of 0.05 M GeO_2 and 0.01 M $Na_2B_4O_7$. Ge ec-LLS was then performed via chronoamperometry with an applied potential of -1.94 V for up to 1 h.

2.2.3 Materials Characterization

Scanning electron microscopy was conducted in a FEI Quanta 3D e-SEM/FIB in low vacuum mode with a pressure of 0.60 torr operated at 5.00-10.00 kV, and a FEI Helios 650 Nanolab SEM/FIB operated at 1.00-3.00 kV. Energy dispersive X-ray measurements were obtained using an EDAX 30 mm^2 SDD detector. All energy dispersive X-ray data are presented as raw signals, i.e. without any adjustment for differences in relative sensitivities.

2.3 Results

2.3.1 Voltammetry

Figure 2.2 displays voltammetry illustrating the efficacy of the process to produce Hg ultramicroelectrodes. Figure 2.2a illustrates the attenuation of the electrocatalytic activity for H^+ reduction in 0.01 M $Na_2B_4O_7$(aq) following electrodeposition of Hg onto a 10 μm diameter Pt ultramicroelectrode. At a current of 10 nA, the overpotential for H_2 evolution increased by nearly 600 mV. The high overpotential was maintained after multiple sweeps, indicating the stability of the Hg microdroplet. The inset to Figure 2.2 highlights a scanning electron micrograph (top-down view) of a typical Hg microdroplet ultramicroelectrode after preparation. Figure 2.2b presents a representative cyclic voltammetric response for a Hg microdroplet ultramicroelectrode with r = 8.9 μm in an aqueous solution containing 0.1 M KCl and 0.001 M $Ru(NH_3)_6Cl_3$. The steady-state current-potential response followed the expected response for a hemispheric ultramicroelectrode.

Figure 2.3 presents representative cyclic voltammograms for the reduction of 0.050 M dissolved GeO_2 in aqueous solution at a Hg microdroplet ultramicroelectrode with r = 8.9 μm. For reference, the standard potential for the $HGeO_3^-$/Ge redox couple is -1.34 V.[20] The data in Figure 2.3a were collected at 0.01 V s^{-1}. An increased faradaic current was consistently observed at potentials more negative than -1.7 V when GeO_2 was dissolved as compared to the blank electrolyte (Figure 2.3a). The peak near E = -1.85 V in Figure 2.3a indicated a transition from kinetic to mass-transport limited current for GeO_2 reduction, in contrast to the voltammetric response at a bulk Hg pool electrode in the same ec-LLS electrolyte at a comparably slow scan rate.[12] At more negative potentials, the current continued to increase. Although a second peak at E = -2.05 V is apparent in Figure 2.3a, this feature was not consistently observed. However, a

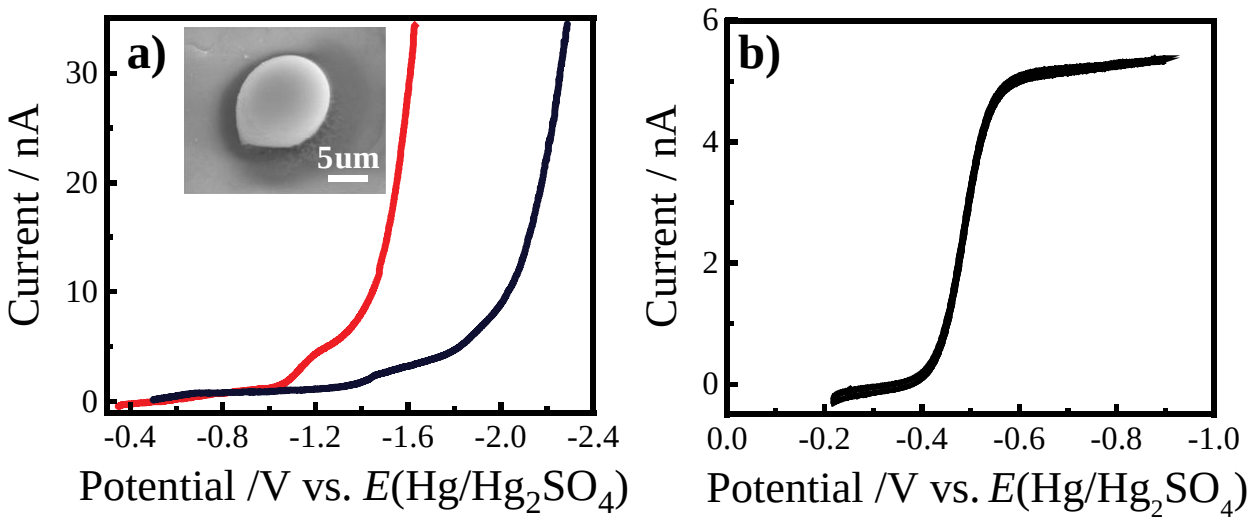

Figure 2.2. a) Comparison of the voltammetric responses in 0.01 M $Na_2B_4O_7$ of a Pt ultramicroelectrode before and after electrodeposition of Hg. Scan rate: 0.01 V s^{-1} Inset: a top-down scanning electron micrograph of a Hg microdroplet ultramicroelectrode. b) Steady-state voltammetric response of a Hg microdroplet ultramicroelectrode immersed in 0.001 M $Ru(NH_3)_6Cl_3$ and 0.1 M KCl. Scan rate: 0.01 V s^{-1}

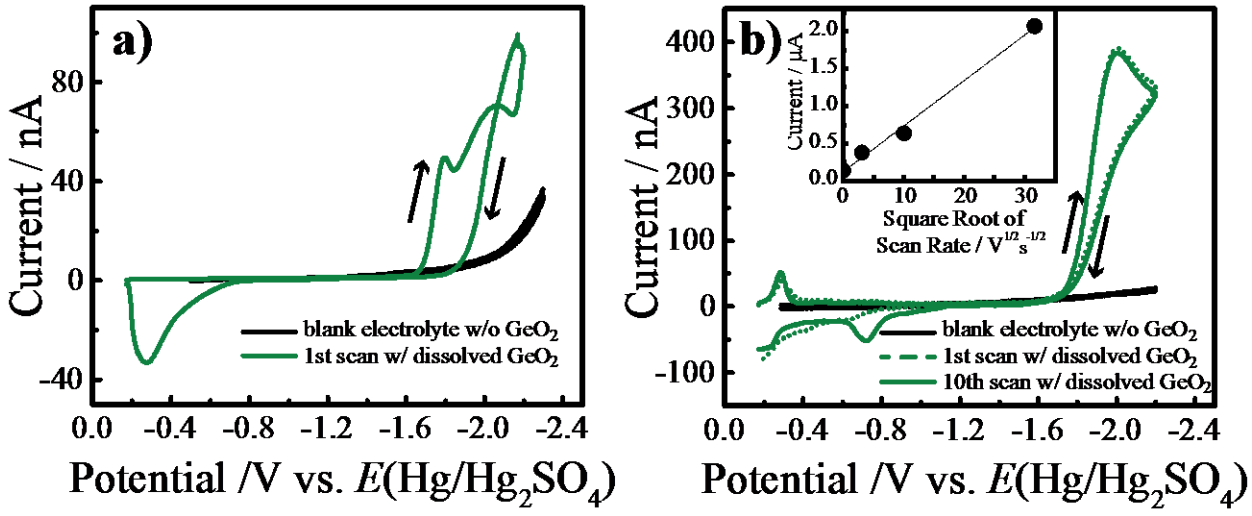

Figure 2.3. a) Comparison of the voltammetric responses of a Hg microdroplet ultramicroelectrode immersed in aqueous 0.01 M $Na_2B_4O_7$ with (green) and without (black) 0.05 M dissolved GeO_2. Scan rate: 0.01 V s^{-1}. b) Comparison of the voltammetric responses of a Hg microdroplet ultramicroelectrode immersed in aqueous 0.01 M $Na_2B_4O_7$ with (green) and without (black) 0.05 M dissolved GeO_2. Scan rate: 10 V s^{-1}. Inset: Plot of peak current of cathodic feature near E = -2 V vs $E(Hg/Hg_2SO_4)$ vs square root of the scan rate. The arrows are visual guides to indicate the scan direction.

prominent feature that is evident in Figure 2.3a that was seen in all voltammetric data recorded at this scan rate was the crossover in the forward and reverse scans. The cathodic current was higher at the most negative potential values on the reverse scan, suggestive that the electrode surface was no longer pure Hg after the reduction of dissolved GeO_2. Rather, the electrode interface featured some fraction of solid Ge which was more electrocatalytically active for H^+ reduction compared with bare Hg. The convolution of the cathodic charge with the electrochemical reduction of H^+ precluded direct comparison of the charge passed between the cathodic and anodic sweeps. At more positive potentials, the anodic sweep contained a broad, asymmetric stripping wave beginning at -0.7 V but with a peak potential nominally located at -0.35 V. This anodic stripping peak was consistent with a voltammetric feature reported previously for the oxidation of solid Ge^0 at hanging Hg drop electrodes used for the electroanalytical detection of Ge.[15, 16, 21] The unusual asymmetry of the peak shape has been described as arising from both the oxidation of solid Ge at the electrolyte interface and from within Hg.[15, 16, 21]

Figure 2.3b presents separate cyclic voltammograms collected at 10 V s^{-1} in the presence of dissolved GeO_2 at a formal concentration of 0.05 M. In these experiments, a cathodic peak at E = -0.28 V and an anodic wave at E= -0.23 V were routinely observed. Separate control experiments were performed to confirm these features were neither associated with an unintentional impurity in solution (e.g. contaminants from the electrolyte salt, dissolved O_2) nor related to the underling presence of Pt below the Hg microdroplet. Instead, these features seemed reminiscent of the formation/removal of polyborate adsorbed layers previously reported on Ag electrodes.[22, 23] Nevertheless, they do not appear at potentials directly or indirectly associated with the reduction of dissolved GeO_2. The first and tenth scans obtained under these conditions

are shown. These two plots are shown to illustrate that some aspects were not constant across multiple scans. One consistent feature was the absence of a crossover in the forward and reverse scans after the reduction wave for dissolved GeO_2. In both the first and tenth scans, the reduction of dissolved GeO_2 appeared as a typical irreversible cathodic wave without convolution with H_2 evolution, suggesting the electrode interface was still uniformly Hg. The dependence of the peak current with the square root of the respective scan rate from 0.01 V s^{-1} to 1000 V s^{-1} was linear (inset), i.e. consistent with the reduction of freely dissolved species in solution rather than adsorbed species. Another common feature in both scans was the absence of a broad anodic stripping wave centered at -0.35 V, further indicating solid Ge had not yet formed even though each cathodic wave indicated the production of 5.5 x 10^{-14} moles of Ge if Reaction 1 was the only operative redox process.

On the first scan, there was minimal anodic current in this potential range. In fact, for all fast voltammetric responses collected, the total anodic charge passed was approximately 20x less than the total cathodic charge passed, particularly since the current at the most positive potentials was broadly in line with the voltammetry for the blank electrolyte shown in Figure 2.3b. After the first scan, a new symmetric oxidative wave appeared, centered at -0.72 V, and was consistent with the oxidative stripping of *dissolved* Ge in Hg, i.e. solvated Ge that has not yet phase separated into a solid Ge crystal.[15, 16] The magnitude of this wave increased with each new scan, until reaching a plateau value by the tenth scan. Assuming this peak is the $2e^-$ oxidation of Ge^0 dissolved in Ge,[15, 16] a maximum of 4.7 x 10^{-15} moles of Ge were apparently dissolved within this Hg microdroplet ultramicroelectrode by the heterogeneous reduction of GeO_2. With a total Hg microdroplet volume (assuming a hemisphere as in Figure 2.2a) of 1.5 x 10^{-9} cm^{-3}, the effective concentration of Ge in the Hg microdroplet after repetitive scanning was

3.2 x 10^{-3} M (4.74 x 10^{-7} mol %). The solubility data for Ge in Hg at room temperature are scattered,[24-27] but the most widely cited value is 10^{-3} M (10^{-7} mol %).[28] The data in Figure 2.3b are thus consistent with the premise that the Hg microdroplet electrodes were not instantaneously but eventually saturated with Ge upon repetitive cycling at fast scan rates.

2.3.2 Chronoamperometry

A total of 35 separate ec-LLS experiments were performed in 0.05 M GeO_2 and 0.01 M $Na_2B_4O_7$ under constant applied potential. Every ec-LLS attempt yielded a solid Ge deposit that extended outside of the liquid metal ultramicroelectrodes. However, there was notable variation in both the electrochemical data recorded during ec-LLS and the morphology of the electrodeposited Ge produced by ec-LLS, i.e. not every experiment performed under identical conditions yielded the same form of elemental Ge.

Figure 2.4 illustrates an example of one subset (10 out of 35) of the total experiments. Figure 2.4a shows the chronoamperometry data for an ec-LLS experiment where a bias of -1.94 V vs $E(Hg/Hg_2SO_4)$ was applied for 1 h. The current decayed slowly until after ~1000 s, when a steady-state, non-zero current of 2.2 nA was reached. During the first 1000 s, a brief rise in the current was observed. The inset shows the corresponding scanning electron micrograph (top-down view) collected immediately after the completion of the electrodeposition experiment. A round mass was still present on top of the Pt disc ultramicroelectrode but it was not composed purely of Hg. The entire surface of the Hg droplet was covered with a thick shell consisting of elemental Ge, as determined by energy dispersive X-ray spectroscopy (Figure 2.4b). The Al, Na, Si, and O signals arose from the soda glass and the Hg signal was from the underlying microdroplet. For this subset of samples, the ‘shell’ was granular in appearance but otherwise

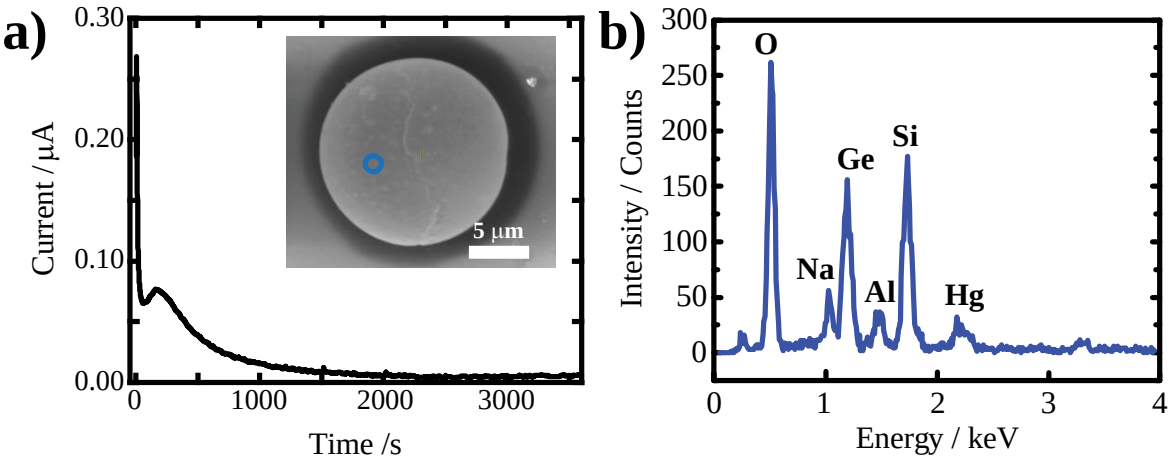

Figure 2.4. a) Current-time transient response for a Hg microdroplet ultramicroelectrode immersed in 0.05 M dissolved GeO_2 and 0.01 M $Na_2B_4O_7$ and biased at E = -1.94 V vs $E(Hg/Hg_2SO_4)$. Inset: a top-down scanning electron micrograph of a Hg microdroplet ultramicroelectrode featuring a Ge shell after ec-LLS. b) Energy dispersive X-ray spectrum of the Ge shell in (a).

continuous. For samples where the Ge ‘shell’ was cracked and a cross-sectional view was possible, a thickness of about 300 nm was apparent.

Figure 2.5 presents data for the other subset (25 out of 35) of ec-LLS experiments attempted with Hg microdroplet ultramicroelectrodes. The current-time profiles for these experiments differed from those shown in Figure 2.4 in two important ways. First, at long times, the current did not reach the same steady-state value. In fact, the majority of these experiments did not attain any steady-state current, with the measured current increasing over time (Figures 2.5a,c). Second, all of the experiments yielded unique current-time profiles. That is, there were no consistent, identifiable patterns. This latter point corroborated the observations from scanning electron microscopy. As demonstrated in Figures 2.5b,d, the resultant morphology was not a Hg droplet covered by a continuous Ge shell. Rather, the collected data for these experiments showed the extrusion of a coiled microwire. In the previous work of Ge ec-LLs at bulk Hg pool electrodes,[12] only large isotropic Ge crystallites or thin, polycrystalline Ge nanowire filaments were observed. Accordingly, the data in Figure 2.5 show unique structures produced by ec-LLS at these Hg microdroplet ultramicroelectrodes.

Figure 2.6 collects higher resolution scanning electron micrographs obtained under high vacuum of an experiment that produced the extruded, coiled structure. Figure 2.6a shows a low magnification view of a structure similar to what is shown in Figure 2.5d, i.e. a hemispherical electrode with a ruptured Ge cap attached by a coiled structure. Figure 2.6b illustrates that the surface of the Ge ‘crust’ is textured and very similar to what was observed at bulk Hg electrodes after Ge ec-LLS was performed at low overpotentials.[12] Figure 2.6c presents a high magnification view of a section of the coil. The surface is highly textured but distinct from that shown in Figure 2.6b. Here the surface presents solid Ge with a branched, ‘leaf’-type pattern.

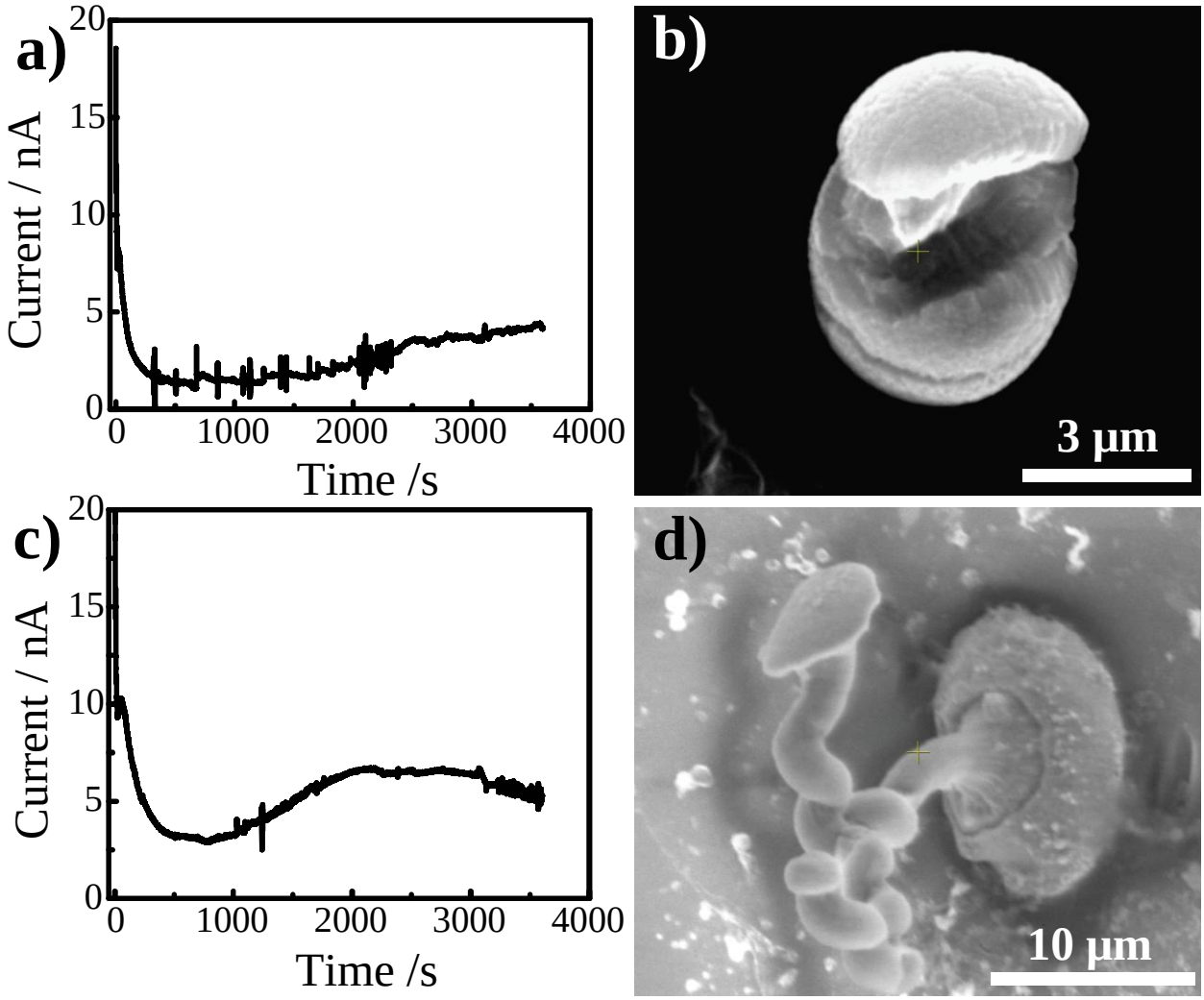

Figure 2.5. a) Current-time transient response for a Hg microdroplet ultramicroelectrode immersed in 0.05 M dissolved GeO_2 and 0.01 M $Na_2B_4O_7$ and biased at E = -1.94 V vs $E(Hg/Hg_2SO_4)$. b) Top-down scanning electron micrograph of a Hg microdroplet ultramicroelectrode after the experiment shown in (a). c) Current-time transient response for a different Hg microdroplet ultramicroelectrode immersed in 0.05 M dissolved GeO_2 and 0.01 M $Na_2B_4O_7$ and biased at E = -1.94 V vs $E(Hg/Hg_2SO_4)$. d) Top-down scanning electron micrograph of a Hg microdroplet ultramicroelectrode after the experiment shown in (c).

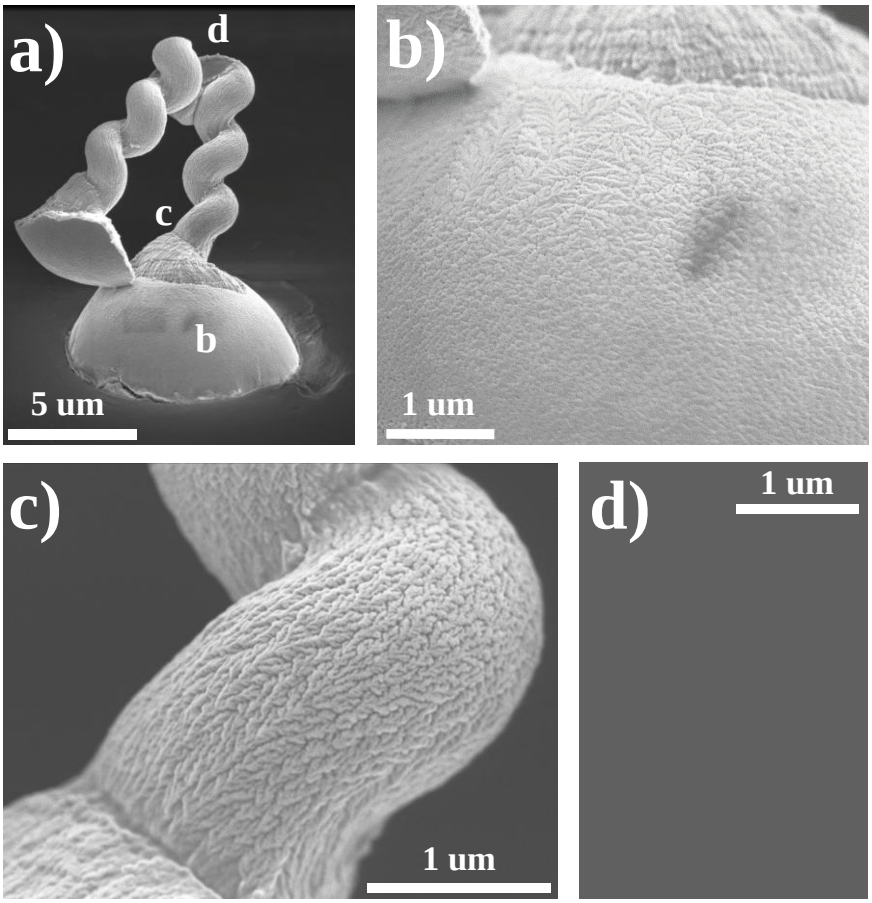

Figure 2.6. Scanning electron micrographs of a Hg microdroplet ultramicroelectrode immersed in 0.05 M dissolved GeO_2 and 0.01 M $Na_2B_4O_7$ after biasing at E = -1.94 V vs $E(Hg/Hg_2SO_4)$ for 60 min. a) Side-view of entire structure. Select regions are shown at higher magnification in (b), (c), and (d), respectively.

Again, a similar pattern was observed previously in Ge ec-LLS at bulk Hg pool electrodes, but only at moderate to large overpotentials.[12] Additionally, the 'leaf' pattern in Figure 2.6c was oriented along the long axis of the coil. Although the coiled Ge structure appears solid in Figure 2.6c, a rupture at the midpoint of the coil revealed this feature was not polycrystalline Ge throughout (Figure 2.6d). Scanning electron micrographs obtained earlier for the same structure at low vacuum (i.e. under conditions where Hg does not evaporate) revealed the core was filled with Hg. As seen in Figure 2.6d, the interior of the hollow coil featured a highly nodular surface. It was not possible to determine whether the origin of the twisted, hollow coil was an intrinsic (i.e. a specific result from how Ge was nucleated) or an extrinsic (i.e. capillary forces acted upon the Ge tube as it was dried following removal from solution) aspect of this growth. Although the pitch of turns per length was similar between samples, the chirality of the coil was not the same throughout all samples.

2.4 Discussion.

The presented data speak to the following three points. First, electrodeposition of solid Ge^0 is possible at discrete Hg microdroplets. However, the voltammetric responses identified a discrepancy between the amount of GeO_2 that is reduced heterogeneously and the amount of Ge dissolved in Hg and an unexpectedly slow saturation of Hg with dissolved Ge. Second, the current transients collected during chronoamperometric ec-LLS experiments with these platforms provide some information on the resultant morphology of the Ge crystals. The limited correlations between the current transients and resultant Ge morphologies argue against precise, real-time feedback control during this type of ec-LLS. Third, the crystalline Ge produced during

ec-LLS has different structural characteristics when performed with Hg microdroplets or Hg bulk pool electrodes. These points are elaborated individually below.

2.4.1 Observations from Voltammetry

The voltammetric data here implicate an unexpectedly slow accumulation of Ge inside Hg. Specifically, the data collected here identify a large discrepancy between the cathodic and anodic charges passed that is not related to the competing evolution of H_2. The much greater cathodic charge passed during the reduction of dissolved GeO_2 in fast scan voltammetry unambiguously shows that only a small fraction of the reduced product results in Ge^0 dissolved in Hg. Although the linear dependence of the peak current on the square root of the scan rate is consistent with the reduction of a GeO_2 species dissolved in the aqueous electrolyte rather than adsorbed on the electrode surface, the possibilities of (*1*) additional redox processes occurring in parallel with Reaction 1 at negative applied potentials, (*2*) undefined coupled chemical reactions that eliminate any freshly produced Ge^0 at the electrode surface, (*3*) the transient formation of a redox inactive Ge-Hg compound, or (*4*) the $4e^-$ reduction of GeO_2 forming a soluble Ge^{2+} intermediate that diffuses away sufficiently fast to yield inefficient production of Ge^0 cannot be ruled out. For example, dissolved GeO_2 could get hydrogenated to form a hydride (e.g. GeH_4)[29] with transient stability in solution. Such a parallel redox process would naturally lower the faradaic efficiency for crystalline Ge formation. Although the generation of Ge hydrides electrochemically has been studied previously, the prevailing sense is this type of hydrogenation is slow and never proceeds with high faradaic efficiency at metal electrodes.[29] The rate of Ge hydride formation at Hg has not been previously reported. A separate possibility is that Ge^0 is produced at the Hg interface but then desorbs (oxidatively) into solution faster than the rate of

dissolution into Hg. The third possibility is that Ge and Hg form a metastable and electroinactive intermetallic species. There is no known precedent for such a compound. In contrast, the formation of a Ge^{2+} intermediate is plausible[15, 16] but substantiation requires a more detailed understanding of the GeO_2 electroreduction process, the reactivity and stabilities of all intermediates, and their diffusivities. Such work is ongoing in our laboratory.

2.4.2 Observations from Chronoamperometry

The current-time data contained some useful information on the initial nucleation and crystal growth during ec-LLS. The slow current decay and peak indicated that Ge electrodeposition occurred over the first 1000 s. After that point, a time-independent current was useful in predicting if a continuous Ge coating was formed. We posit that a continuous Ge shell effectively stopped further Ge ec-LLS, as the electrodeposition of Ge on Ge is not possible under the employed conditions.[30] The residual current was likely from some non-zero rate of H^+ reduction on Ge at the applied potential. Conversely, if the current rose slowly over time after the first 1000 s, a pierced/broken/discontinuous Ge shell was routinely observed. In that aspect, the current-transients were consistent. However, for these ec-LLS experiments, both the current transients and the corresponding Ge deposits were unique and without any discernible patterns. Nothing in the current-time profiles seemed to indicate how or when the Ge nanofilament bundles were extruded. Additionally, there were no apparent periodic oscillations in the chronoamperometry data that followed the periodicity of the twists in the Ge nanofilament bundles. As a result, these data do not support the premise that a simple analysis of the current-time transient in an ec-LLS experiment is a precise indicator of the morphology of the solid that is produced when a Hg microdroplet is used.

With regards to formation of crystalline Ge, the results shown here with Hg microdroplets illustrate some important similarities and differences to liquid Ga and Ga-In alloy liquid metal microdroplet electrodes.[10, 13, 14] In general, the data shown here further emphasize that ec-LLS can be a synthetic materials method at the micro-, meso-, and macro- length scales. However, with liquid Ga or Ga-In microdroplets, the growing Ge crystal(s) push the liquid metal nano/microdroplet away from the surface because nucleation and crystal growth occur preferentially at the interface between the liquid metal droplet and the support substrate. Accordingly, such ec-LLS experiments necessarily involve a moving boundary as the position of the active electrode interface changes with time. In contrast, none of the trials in this work yielded a Hg microdroplet pushed away from the underlying Pt microdisk substrate. Instead, the data all are in line with Ge extruding out of the Hg microdroplet, perhaps because Ge nucleated and grew from inside Hg rather than at the interface between Hg and Pt.

The Hg microdroplet remained attached to the Pt ultramicroelectrode throughout the electrodeposition processes shown here. Strong adhesion of the Hg microdroplets on Pt are in line with the finite solubility of Pt in Hg at room temperature (10^{-4} mol% at T= 25 °C).[31] The possibility exists that an amalgamated bottom interface specifically prevented the heterogeneous Ge nucleation and crystal growth observed previously with Ga microdroplets. To explore this point further, additional ec-LLS experiments were performed with Hg microdroplets electrodeposited on a degenerately doped n^+-Si wafer since there is no metallurgy or wetting of Hg on Si at T = 25 °C.[28] For these experiments, there was no possibility of an amalgam forming that could prevent heterogeneous Ge nucleation and growth. After ec-LLS experiments, *none* of these Hg microdroplets were displaced away from the substrate, arguing against an amalgam adhesion layer as the reason the Hg microdroplet remained in contact with the Pt

ultramicroelectrode during ec-LLS. Instead, these data implicate some specific property of Hg itself as the reason why heterogeneous nucleation did not occur as has been observed previously with other types of liquid metal microdroplets. One property that could have a strong influence is the solvent power of the liquid metal. The solubility of Ge in Hg is 10,000 times less than Ge in Ga at T = 25°C (10^{-7} mol% vs 10^{-3} mol%, respectively).[31, 32] Based on this fact alone, Ge crystal nucleation and growth should start sooner in Hg than Ga during a set of otherwise identical ec-LLS experiments, perhaps making it difficult for crystal growth to occur far from the liquid metal/electrolyte interface when Hg is used.

2.4.3. Comparison of Ge ec-LLS at Micro and Macro Liquid Hg Droplets

This work indicates several clear distinctions between ec-LLS experiments with Hg microdroplets and bulk Hg pools. First, in our past work with bulk pool Hg electrodes, cessation of Ge ec-LLS by the formation of a continuous solid shell never occurred. That is, the amount of Ge deposited always tracked with charge passed and was unabated over long times (> 8 h). In contrast, ec-LLS experiments with the Hg microdroplet ultramicroelectrodes here showed a substantially higher probability for the formation of a solid Ge shell that precluded deposition at long times. To be clear, a Ge shell was also observed with bulk Hg pool electrodes, but the distinction was that it served as a nucleating point for polycrystalline Ge nanowires but never fully encapsulated the bulk Hg pool.

The data indicated that Ge ec-LLS involves a compressive force on the liquid metal that can disrupt the initial Ge shell. It is presently unclear whether that force is more prominent at a macroscopic Hg electrode interface, but the data suggest that it is a pathway for ‘fresh’ Hg to remain in contact with the electrolyte solution. Accordingly, it seems the probability that such

events could scale with surface area and thus be the reason why ec-LLS at large Hg pool electrodes is always continuous.

Second, the compression of the liquid Hg, in conjunction with the small finite volumes, also facilitated the deposition of unique Hg-filled Ge microtube structures that were never observed with bulk Hg pool electrodes. In fact, such morphologies have not been observed in any other electrodeposition context, ec-LLS or otherwise. Although there might not be an immediate application for the specific hollow Ge structures prepared here, the data shown in the report illustrate the unusual and unexplored concept of using compressed liquid metal electrodes to form unique hollow structures. Accordingly, this phenomenon could be exploited purposefully in the future to synthesize electrochemically hollow micro- or macrostructures.

2.5 Conclusion.

In this work, small Hg microdroplet ultramicroelectrodes facilitated Ge ec-LLS through the reduction of aqueous solutions of dissolved GeO_2. The voltammetric data suggest a complex interplay between the reduction of dissolved GeO_2 and the dissolution of Ge into Hg. Chronoamperometric experiments showed the formation of continuous Ge shells, an observation never seen before in ec-LLS with either large volume Hg electrodes or similarly sized Ga microdroplet ultramicroelectrodes. The formation of Hg-filled, crystalline Ge coil structures at long times was unprecedented and suggests the possibility of synthesizing unique hollow structures by electrodeposition.

2.6 Acknowledgements.

The authors acknowledge funds from the National Science Foundation (CHE-1505635) in support of this work, as well as A. Hunter of the Michigan Center for Materials Characterization for assistance with the FEI Helios 650 nanolab SEM/FIB.

2.7 References

1. R. S. Wagner and W. C. Ellis, *Appl. Phys. Lett.*, **4**, 89 (1964).
2. B. A. Wacaser, K. A. Dick, J. Johansson, M. T. Borgström, K. Deppert and L. Samuelson, *Adv. Mater.*, **21**, 153 (2009).
3. A. D. Gamalski, C. Ducati and S. Hofmann, *J. Phys. Chem. C*, **115**, 4413 (2011).
4. F. Wang, A. Dong, J. Sun, R. Tang, H. Yu and W. E. Buhro, *Inorg. Chem.*, **45**, 7511 (2006).
5. T. J. Trentler, K. M. Hickman, S. C. Goel, A. M. Viano, P. C. Gibbons and W. E. Buhro, *Science*, **270**, 1791 (1995).
6. G. Cao and D. Liu, *Adv. Colloid Interface Sci.*, **136**, 45 (2008).
7. J. Mallet, M. Molinari, F. Martineau, F. Delavoie, P. Fricoteaux and M. Troyon, *Nano Lett.*, **8**, 3468 (2008).
8. J. Chun and J. Lee, *Eur. J. Inorg. Chem.*, **2010**, 4251 (2010).
9. S. Barth, F. Hernandez-Ramirez, J. D. Holmes and A. Romano-Rodriguez, *Prog. Mater. Sci.*, **55**, 563 (2010).
10. E. Fahrenkrug and S. Maldonado, *Acc. Chem. Res.*, **48**, 1881 (2015).
11. E. Fahrenkrug, J. Biehl and S. Maldonado, *Chem. Mater.*, **27**, 3389 (2015).
12. A. I. Carim, S. M. Collins, J. M. Foley and S. Maldonado, *J. Am. Chem. Soc.*, **133**, 13292 (2011).
13. E. Fahrenkrug, J. Gu, S. Jeon, P. A. Veneman, R. S. Goldman and S. Maldonado, *Nano Lett.*, **14**, 847 (2014).
14. L. Ma, J. Gu, E. Fahrenkrug and S. Maldonado, *J. Electrochem. Soc.*, **161**, D3044 (2014).
15. Z. J. Karpiński and Z. Kublik, *J. Electroanal. Chem. Inter. Electrochem.*, **81**, 53 (1977).
16. Z. J. Karpiński and Z. Kublik, *J. Electroanal. Chem. Inter. Electrochem.*, **106**, 47 (1980).
17. J. Mauzeroll, E. A. Hueske and A. J. Bard, *Anal. Chem.*, **75**, 3880 (2003).
18. L. Libioulle, Y. Houbion and J. M. Gilles, *Rev. Sci. Instrum.*, **66**, 97 (1995).
19. C. G. Zoski, *Electroanal.*, **14**, 1041 (2002).
20. M. Pourbaix, *Atlas of electrochemical equilibria in aqueous solutions*, p. 644, National Association of Corrosion Engineers, Houston, Tex. (1974).
21. Z. J. Karpiński and Z. Kublik, *J. Electroanal. Chem. Inter. Electrochem.*, **226**, 331 (1987).
22. K. J. Stevenson, D. W. Hatchett and H. S. White, *Langmuir*, **13**, 6824 (1997).
23. M. Hepel, K. Kanige and S. Bruckenstein, *Langmuir*, **6**, 1063 (1990).
24. J. F. Strachan and N. L. Harris, *J. I. Met.*, **85**, 17 (1956).
25. V. P. Gladyshev, S.V. Kovaleva, and L.S. Sarieva, *Zh. Anal. Khim.*, **37**, 1762 (1982).
26. O. S. Stepanova and M.S. Zakharov, *Izv. Tomsk. Politekh. Inst.*, **151**, 21 (1966).
27. O. S. Stepanova and M.S. Zakharov, *Elektrokhimiya*, **2**, 777 (1966).
28. C. Guminski, *J. Phase Equilib.*, **20**, 344 (1999).
29. V. V. Turygin, A. P. Tomilov, M. Y. Berezkin and V. A. Fedorov, *Inorg. Mater.*, **46**, 1459 (2010).
30. G. Szekely, *J. Electrochem. Soc.*, **98**, 318 (1951).
31. C. Gumiński, *J. Mater. Sci.*, **24**, 2661.
32. P. H. Keck and J. Broder, *Phys. Rev.*, **90**, 521 (1953).

Chapter 3

Comparison of the Voltammetric Responses for Ion Adsorption/Desorption at Hg Macroelectrodes and Ultramicroelectrodes

3.1 Introduction

This chapter describes the adsorption and desorption of charged electrolyte species on macroscale bulk Hg pool electrodes and Hg microdroplet ultramicroelectrodes through cyclic voltammetry. The aim of the work is to determine if the larger surface-to-volume ratios in Hg ultramicroelectrodes cause any noticeable change in the voltammetric responses of adsorbates. The key motivation is to determine if there are any distinguishing features at microdroplets relative to bulk pools that would complicate/perturb surface-driven processes like electrodeposition. Two factors could have relevance. First, mass transport is faster at microdroplets because (hemi)spherical diffusion rather than planar diffusion is operative. Second, the inherent electrocapillarity of liquid metal electrodes may be more disruptive to surface adsorption when the surface to volume ratio is large.

The mass transport effect at microelectrodes is well described.[1-3] However, the electrocapillarity action of liquid metal ultramicroelectrodes has received little attention. Electrocapillarity is the deformation of a liquid metal electrode in an electrochemical cell that is caused by changes in the surface charge density.[4-6] Specifically, as the potential of the liquid metal electrode is biased away from the potential of zero charge (*pzc*), the surface tension of the

liquid metal/electrolyte interface necessarily changes and exerts a force on the entire volume of liquid metal.[4,7] A consequence of this phenomenon is that the shape of the liquid metal can be substantially altered. When an ac waveform is applied to the potential of a macroscopic Hg pool electrode, the Hg shape can oscillate in response to the frequency of the waveform.[8-10] However, the frequency and magnitude of oscillations in the shape of the Hg electrode depend strongly on the magnitude of the potentials with respect to the *pzc*, the frequency of the waveform, and the mass of the liquid metal volume.[10] For a given set of conditions, particularly the Hg electrode size, there will be a set of resonant frequencies in the excitation waveform that will induce the most drastic oscillations in the shape of Hg. This effect has been demonstrated numerous times over, most practically in the context of designing a pump based on a small volume of Hg acting as an electrochemically modulated 'piston'.[11-13]

In the context of electrodeposition processes like ec-LLS at small liquid metal volumes (where some initial surface adsorption of species must precede any dissolution into the liquid metal), it is not clear based on theory whether electrocapillarity impacts crystal nucleation and growth. More generally, any surface phenomenon such as electrodeposition or adsorption/desorption may be affected by electrocapillarity at small liquid volumes.

In this work, we choose three types of adsorbates that form films on Hg electrodes as a function of potential and thus elicit a detectable signal in current (i) – potential (E) data plots. The underlying source of the signals in the voltammetry is not based on the reduction of a freely diffusing species. Instead, the investigated redox involves a charged adlayer. Despite the historical precedence of ion adsorption at Hg electrodes[14-18], there are no previous investigations detailing whether size (and more generally electrocapillarity) affects adsorption on Hg.

The three adsorbate types used in this chapter include Br^- (a typical anionic adsorbate[19]), heptyl viologen (a cationic adsorbate),[20] and polyborates (anionic adsorbates composed of oligomers of borate species).[21] These compounds span a 'continuum' representing adsorbates that either bind quickly or slowly due to the lack/presence of preceding/follow-up reactions.

The voltammetry for the deposition and stripping of crystalline adsorbate films on electrodes has been described previously and modeled in detail.[22-24] The expected relationship between the peak current, i_p, and the scan rate, v, in the voltammetric responses for such systems is given by Equation *3.1*,[22]

$$i_p = \frac{q_m 4^{4/5} (^2/_3 \pi (^{RT}/_{nF})^2 k_0^2 B)^{1/5}}{(^{RT}/_{nF}) e^{4/5}} v^{3/5} \qquad (3.1)$$

where q_m is the total charge exchanged, *R* is the ideal gas constant, *T* is the temperature, *n* is the moles of electrons, *F* is Faraday's constant, k_0 is the standard heterogeneous rate constant in cm s^{-1}, *B* is the number of nuclei formed per unit surface as a function of overpotential at low scan rates, and *e* is Euler's number. This relationship will be used to gauge whether the voltammetry indicates the adsorbate responses are behaving in accord with classical expectations (i.e. no perturbation) or if all adsorbates on liquid Hg microdroplets show character that does not follow Equation *3.1*.

This chapter posits one primary hypothesis – the adsorption of species at small Hg electrodes is perturbed systematically by forces that are more significant at the microscale than the macroscale. The polyborate adsorption is also interesting to our lab as it is the most commonly used electrolyte buffer for Ge ec-LLS, and prior voltammetric measurements showed pronounced voltammetric features that suggested polyborate binding (see Chapter 2, Figure 2.3) that hasn't been observed previously.

3.2 Experimental

3.2.1 Materials

25 μm diameter Pt wire (99.95%) was obtained from Alfa Aesar. $CaCl_2$ (97%, Fluka), C_3H_6O (ACS grade, Fisher), $Hg(NO_3)_2$ (98%, Alfa Aesar), KNO_3 (99%, Acros Organics), HNO_3 (65% Fisher Scientific), Ar(g) (99.998%, Detroit Metro Welding), $Na_2B_4O_7$ (≥99.5%, Sigma-Aldrich), NaBr (99.7% J.T. Baker Chemicals), Hg (instrument grade / triple distilled, D.F. Goldsmith), $Hg(NO_3)_2$ (98%, Alfa Aesar), $C_{24}H_{38}Br_2N_2$ (97%, Aldrich), and KBr (≥99%, Sigma-Aldrich) were used as received. Water (Barnstead Nanopure) with a resistivity > 18 MΩ cm was used throughout. Bulk Hg pool electrodes had an effective radius, *r*, of 0.36 cm. Hemispherical Hg microdroplet ultramicroelectrodes possessed *r* values ranging from 5 to 9 μm. The preparation of Hg ultramicroelectrodes is detailed in Chapter 2.

3.2.2 Methods

CH Instruments models 420a and 760c potentiostats, and three electrode cells were used in all electrochemical experiments. All potentials are referenced to a mercury/mercurous sulfate ($E(Hg/Hg_2SO_4)$) reference electrode.

3.3 Results

3.3.1 Bromide Adsorption/Desorption

Figure 3.1 shows the cyclic voltammetric responses of a bulk Hg pool electrode in 0.05 M NaBr(aq) at 10 mVs^{-1} and 100 mV s^{-1}. Unless noted otherwise, the presented cyclic voltammetric data consist of four consecutive cycles overlaid on each other. At both scan rates (v), the cathodic and anodic peak for the expulsion and formation of the anion layer respectively can be observed. However, the peak shapes broadened at the higher scan rate. In Figure 3.1a, the

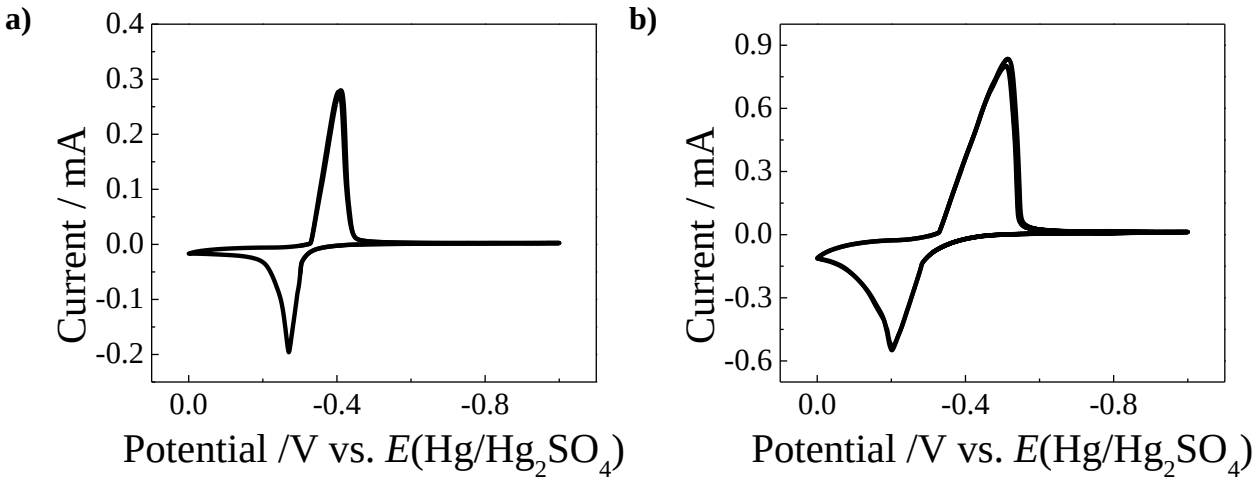

Figure 3.1 Voltammetric response of a bulk Hg pool electrode immersed in 0.050 M NaBr(aq) at scan rates of a) 10 mV s^{-1} and b) 100 mV s^{-1}.

cathodic peak occurred at E = -0.41 V and the peak width at half height was 57 mV. The anodic peak occurred at E = -0.27 V and the peak width at half height was 45 mV. For Figure 3.1b, the cathodic peak occurred at E = -0.51 V and the peak width at half height was 129 mV. The anodic peak was at E = -0.20 V and the peak width at half height was 124 mV. The integrated charge of the cathodic peak corresponded to a surface coverage of 4.1 x 10^{-8} mol cm^{-2} for 10 mV s^{-1} and 2.6 x 10^{-8} mol cm^{-2} for 100 mV s^{-1}.

Figure 3.2 shows the cyclic voltammetric responses of a Hg ultramicroelectrode with r = 8.2 μm in the same solution as Figure 3.1 at scan rates of 10 mV s^{-1} and 100 mV s^{-1}. At both slow and fast scan rates, the absorption and desorption peaks are noticeably more narrow than in Figure 3.1. In Figure 3.2a, the cathodic peak was at E = -0.34 V and the peak width at half height was 16 mV. The anodic peak occurred at E = -0.30 V and the peak width at half height was 6 mV. In Figure 3.2b, the cathodic peak was at E = -0.35 V and the peak width at half height was 23 mV. The anodic peak was at E = -0.30 V and the peak width at half height was 9 mV. The integrated charge of the cathodic peak corresponded to a surface coverage of 4.4 x 10^{-8} mol cm^{-2} for 10 mV s^{-1} and 2.5 x 10^{-8} mol cm^{-2} for 100 mV s^{-1}.

Figure 3.3 shows log-log plots of the peak cathodic current against scan rate for measurements in 0.05 M NaBr(aq) for both Hg electrode types. The data were linear with a slope of 0.42 and 0.58 for the Hg bulk pool electrode and Hg ultramicroelectrode, respectively.

3.3.2 Heptyl Viologen Adsorption/Desorption

Figure 3.4 shows the cyclic voltammetric response of a bulk Hg pool in a 0.001 M $C_{24}H_{38}Br_2N_2$ and 0.1 M KBr solution at scan rates of 10 mV s^{-1} and 100 mV s^{-1}. The peaks are due to the reduction of adsorbed heptyl viologen dications. In Figure 3.4a, the cathodic peak was

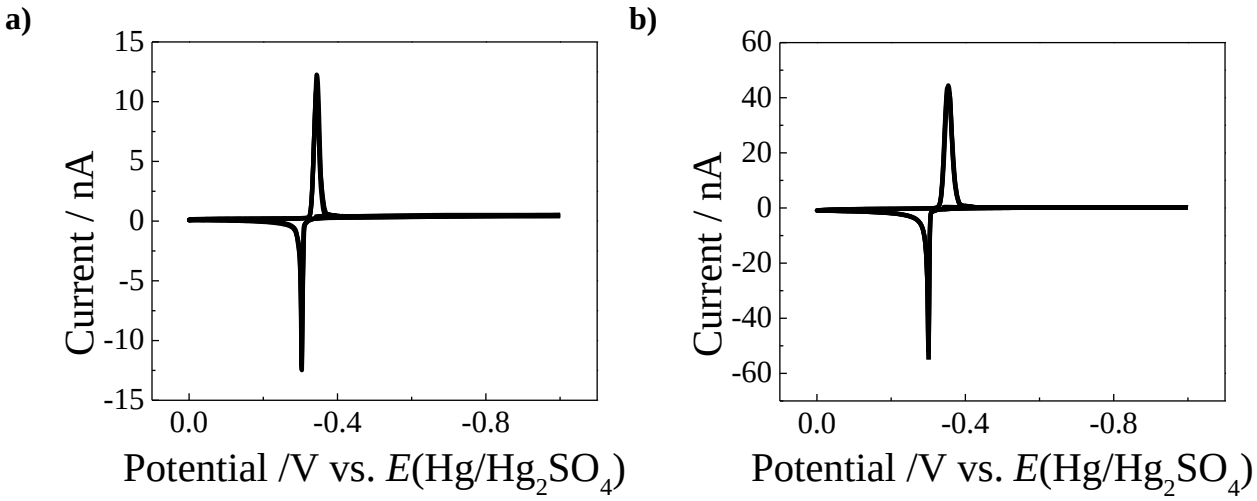

Figure 3.2 Voltammetric response of a Hg ultramicroelectrode immersed in 0.05 M NaBr(aq) at scan rates of a) 10 mV s^{-1} and b) 100 mV s^{-1}.

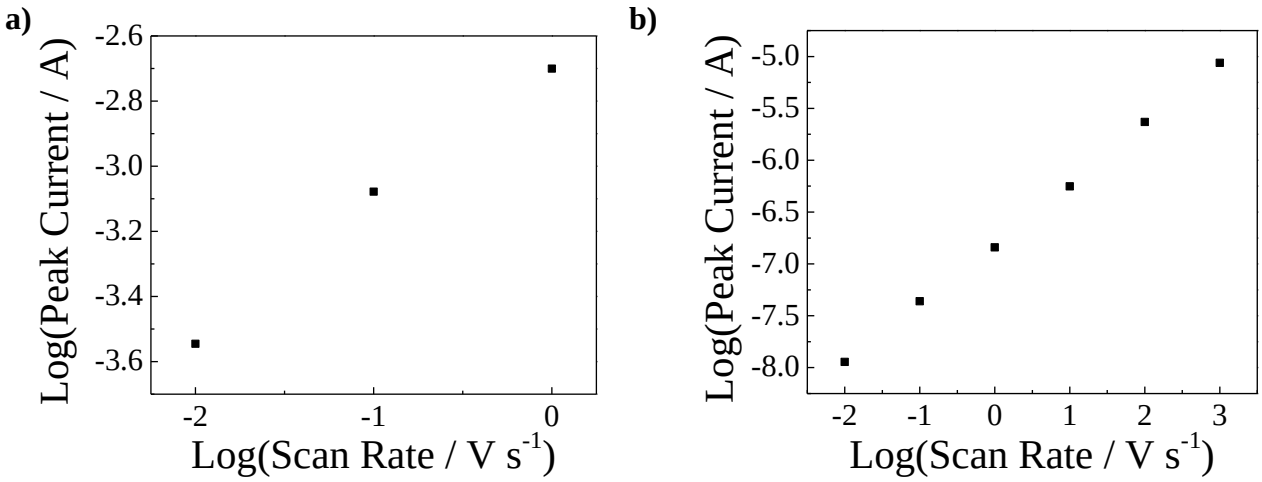

Figure 3.3 Logarithmic plot of peak cathodic current vs scan rate for a) the bulk Hg pool electrode and b) the Hg ultramicroelectrode immersed in 0.050 M NaBr(aq).

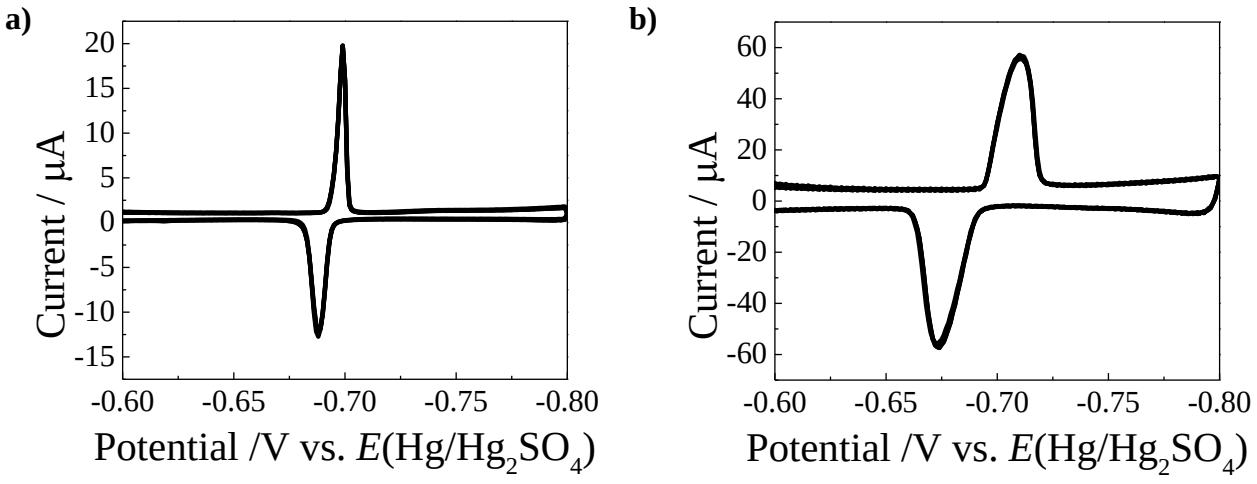

Figure 3.4 Voltammetric response of a bulk Hg pool electrode immersed in 0.001 M $C_{24}H_{38}Br_2N_2$ and 0.1 M KBr at scan rates of a) 10 mV s^{-1} and b) 100 mV s^{-1}.

at E = -0.70 V and the peak width at half height was 4 mV. The anodic peak was at E = -0.69 V and the peak width at half height was 6 mV. In Figure 3.4b, the cathodic peak was at E = -0.71 V and the peak width at half height was 17 mV. The anodic peak was at E = -0.67 V and the peak width at half height was 17 mV. The integrated charge of the cathodic peak corresponded to a surface coverage of 1.0 x 10^{-10} mol cm^{-2} for both 10 mV s^{-1} and 100 mV s^{-1}.

Figure 3.5 shows the cyclic voltammetric response of a Hg ultramicroelectrode with r = 5.8 μm in the same solution as Figure 3.4 at scan rates of 10 mV s^{-1} and 100 mV s^{-1}. In general, the voltammetric features in Figure 3.5 mirrored those in Figure 3.4, except the background currents showed a more resistive character (albeit with much smaller absolute currents). In Figure 3.5a, the cathodic peak is at E = -0.69 V and the peak width at half height was 2 mV. The anodic peak was at E = -0.69 V and the peak width at half height was 9 mV. In Figure 3.5b, the cathodic peak was at E = -0.69 V and the peak width at half height was 11 mV. The anodic peak was at E = -0.69 V and the peak width at half height was 3 mV. The integrated charge of the cathodic peak corresponded to a surface coverage of 7.2 x 10^{-11} mol cm^{-2} for 10 mV s^{-1} and 5.2 x 10^{-11} mol cm^{-2} for 100 mV s^{-1}.

Figure 3.6 shows log-log plots of the peak cathodic current and scan rate collected in the same solution for both Hg electrode types. The plot was linear with a slope of 0.53 for the bulk Hg pool electrode. The plot was linear with a slope of 0.72 for the Hg ultramicroelectrode.

3.3.3 Polyborate Adsorption/Desorption

Figure 3.7 shows the cyclic voltammetric response of a bulk Hg pool electrode immersed in 0.05 M $Na_2B_4O_7$ at scan rates of 10 mV s^{-1} and 10 V s^{-1}. There was a cathodic peak at E = -0.2 V but unlike the other two adsorbates it was not sharp at slow or fast scan rates. There was a

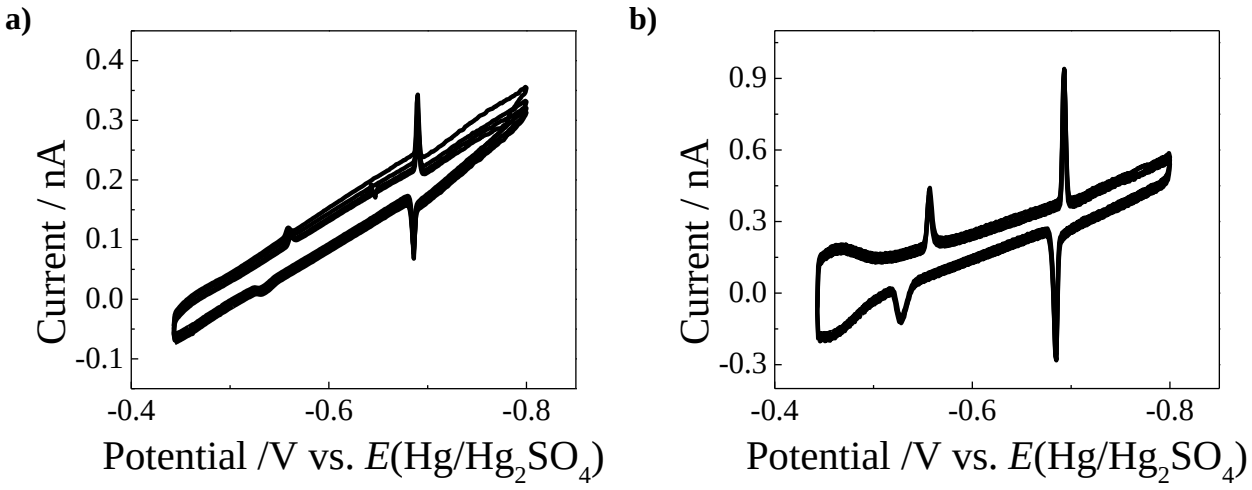

Figure 3.5 Voltammetric response of a Hg ultramicroelectrode immersed in 0.001 M $C_{24}H_{38}Br_2N_2$ and 0.1 M KBr at scan rates of a) 10 mV s^{-1} and b) 100 mV s^{-1}.

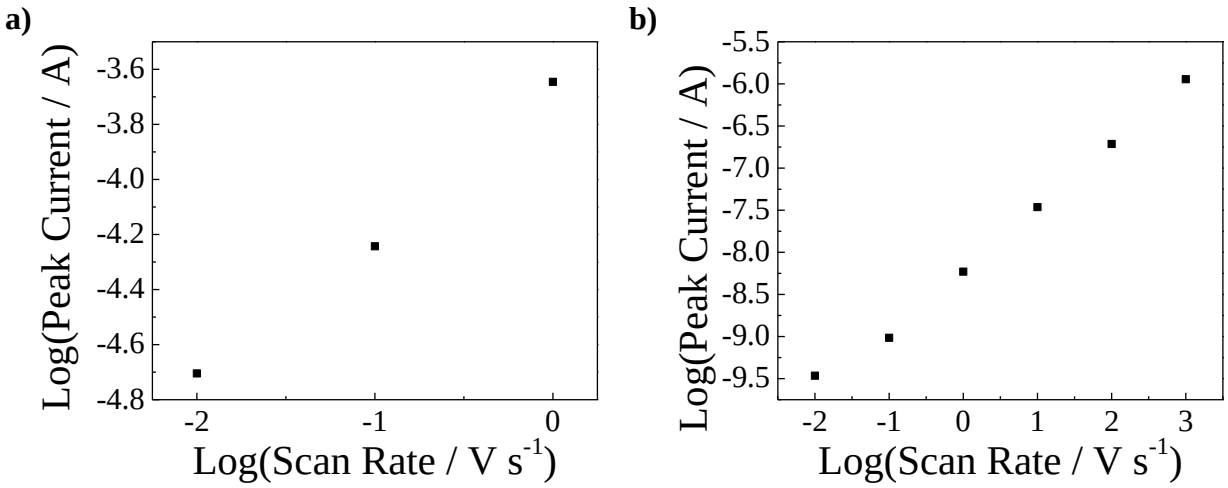

Figure 3.6 Logarithmic plot of peak cathodic current vs scan rate for a) the bulk Hg pool electrode and b) the Hg ultramicroelectrode immersed in 0.001 M $C_{24}H_{38}Br_2N_2$ and 0.1 M KBr.

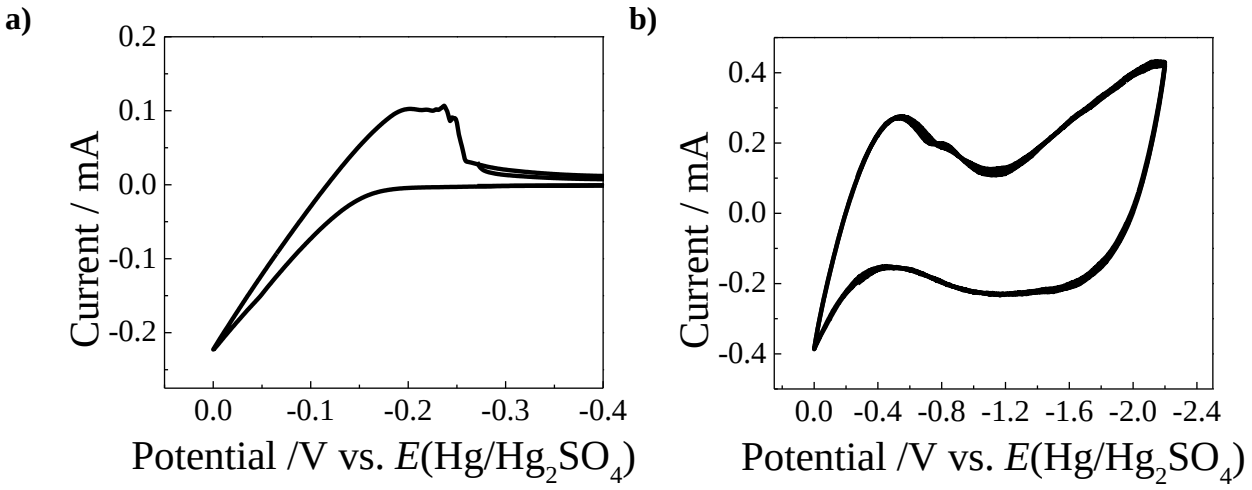

Figure 3.7 Voltammetric response of a bulk Hg pool immersed in 0.05 M $Na_2B_4O_7$ at scan rates of a) 10 mV s^{-1} and b) 10 V s^{-1}.

large anodic current starting at E = -0.1 V, but the potential was not scanned out further because potentials more positive than 0 V caused the electrochemical oxidation of Hg.

Figure 3.8 shows the cyclic voltammetric response for a Hg ultramicroelectrode with r = 8.4 μm in the same solution as Figure 3.7 at 10 mV s^{-1} and 10 V s^{-1}. In comparison to Figure 3.7, the data in Figure 3.8 were significantly different. In Figure 3.8a, sharp peaks were visible in both scan directions. However, the peaks were both net anodic and centered at ~ E = -0.1 V. In the negative sweep, a small cathodic peak at E = -0.2 V was also observed. In Figure 3.8b, the voltammetric features were markedly different. There was a very prominent cathodic peak centered at -0.19 V and there were two apparent anodic peaks at E = –0.13 V and E = -0.09 V. The anodic waves were more pronounced and narrower at the fast scan as compared to the slow scan response.

Figure 3.9 shows log-log plots of the peak cathodic current against the scan rate for three different concentrations of $Na_2B_4O_7$. None of these plots showed a monotonic linear trend across the entire scan rate range. Instead, the trends showed a discontinuity at scan rates slower than 1 V s^{-1}. Below this scan rate, the peak current was nominally invariant to scan rate. Above this scan rate, the peak cathodic current was linearly dependent with a slope of 0.45 for 0.01 M $Na_2B_4O_7$, 0.50 for 0.05 M $Na_2B_4O_7$, and 0.57 for 0.1 M $Na_2B_4O_7$.

Figure 3.10 shows the voltammetry at a scan rate of 10 V s^{-1} for a Hg ultramicroelectrode in three solutions containing different formal concentrations of NaB_4O_7. The anodic and cathodic wave shapes changed dramatically as a function of concentration, becoming sharpest at 0.1 M.

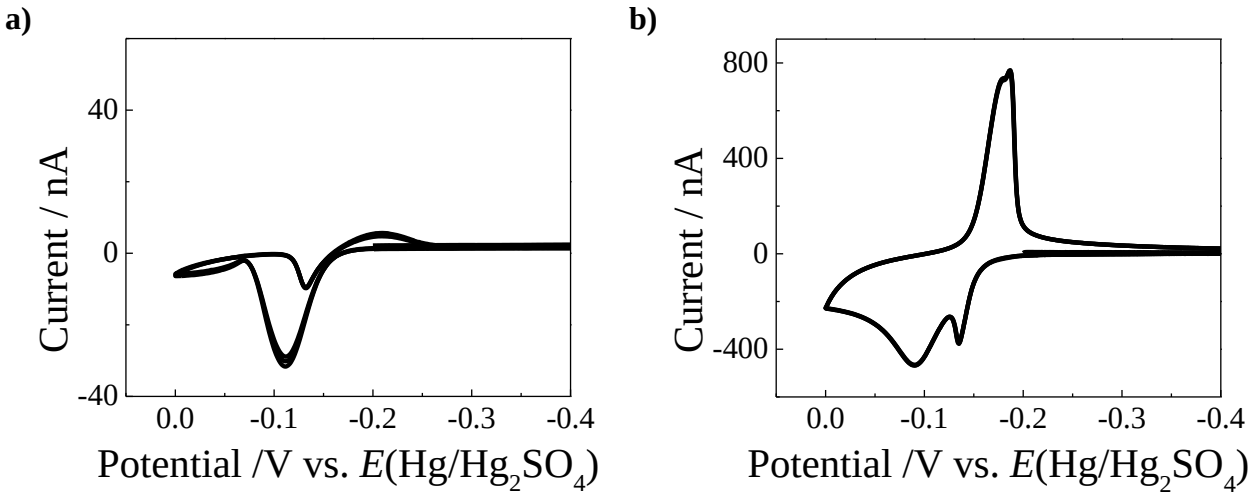

Figure 3.8 Voltammetric response of a Hg ultramicroelectrode immersed in 0.05 M $Na_2B_4O_7$ at scan rates of a) 10 mV s^{-1} and b) 10 V s^{-1}.

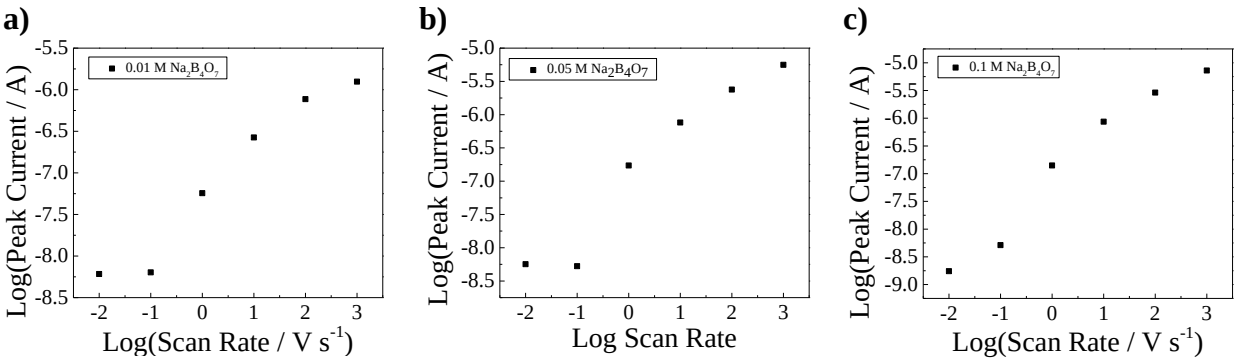

Figure 3.9 Logarithmic plot of peak cathodic current vs scan rate for a Hg ultramicroelectrode immersed in a) 0.01 M $Na_2B_4O_7$, b) 0.05 M $Na_2B_4O_7$ c) 0.1 M $Na_2B_4O_7$.

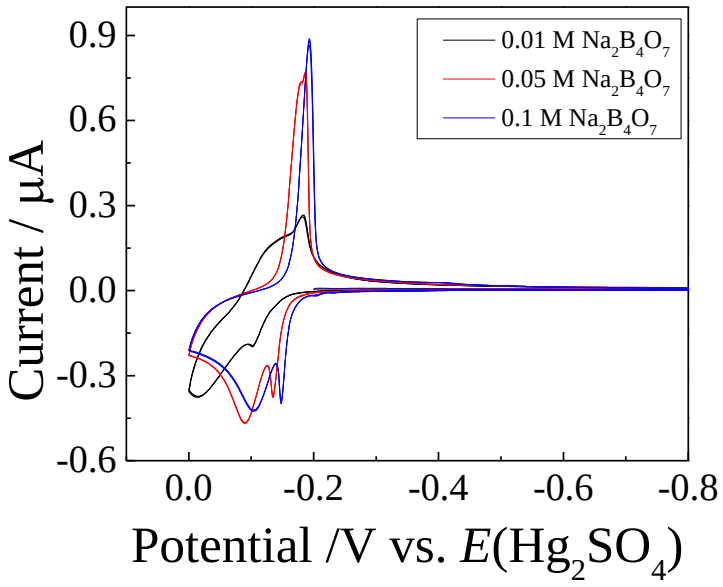

Figure 3.10 Voltammetric response of a Hg ultramicroelectrode at a scan rate of 10 V s^{-1} in 0.01 M $Na_2B_4O_7$ (black), 0.05 M $Na_2B_4O_7$ (red), and 0.1 M $Na_2B_4O_7$.

3.4 Discussion

The presented data highlight individual and global differences in the voltammetric responses for the selected adsorbates on macroscale and microscale liquid Hg electrodes. The differences in each respective case are discussed and then the responses in totality are assessed.

3.4.1 Bromide

The voltammetric responses with a macroscale Hg pool electrode and a Hg ultramicroelectrode have many common features. The voltammetric response for the adsorption/desorption of the Br^- occurred at the same potential and no other signals were measured in the interrogated potential range, including the electroreduction of H^+. The latter observation is important since it confirms the Hg ultramicroelectrode did not suffer from any unintended contributions from the underlying Pt, which would have been shown in increased electrocatalytic activity for H_2 evolution.

The similarities of the voltammetric response suggest the following is occurring at both Hg electrode types. The general reaction sequence for halide adsorption onto Hg is described as an adsorptive step followed by reaction with oxidized Hg atoms at the surface.[19,25,26]

$$X^-(aq) \rightleftarrows X^-_{ads} \qquad (3.2)$$

$$Hg \rightleftarrows Hg^+_{ads} + 1e^- \qquad (3.3)$$

$$2Hg^+ + 2X^-_{ads} \rightleftarrows Hg_2X_2 \qquad (3.4)$$

In the case of Br^-, the formation of crystalline Hg_2Br_2 layer is likely as the solubility of this compound is quite low in water.[27] Accordingly, the anodic voltammetric waves describe the sequential adsorptive, crystallization formation of a crystalline surface layer(s) while the cathodic wave describes a sequential reductive expulsion of the Br^- from the surface.

Nevertheless, the specific attributes of the Br^- adsorption/desorption were different at the macro- and microelectrodes in two noticeable respects. First, at every interrogated scan rate, the widths of the anodic (adsorptive) and cathodic (desorptive) waves were substantially narrower with the Hg ultramicroelectrode. Second, the slope of the linear fit of the log-log plot of the peak cathodic currents vs. scan rate was smaller at the macroscale Hg electrode.

Neither the difference in peak width nor the difference in slope of the log-log plots is consistent with an electrocapillarity effect that perturbs/prevents adsorption-desorption at the smaller ultramicroelectrode. Instead, both features are likely a result of more substantial distortion experienced by the macroscale electrode due to the uncompensated resistances in the low ionic strength media.

3.4.2. Heptyl Viologen

The voltammetric response for the first reduction of heptyl viologen (HV^{2+}) at Hg is known to contain two features. The outer-sphere reduction of dissolved HV^{2+} occurs at E^0 = -0.6 V vs. a saturated calomel electrode (SCE).[28] However, HV^{2+} will also adsorb onto Hg due to the hydrophobicity of the two heptyl chains.[20,29] The adsorbed HV^{2+} can undergo reduction at a substantial underpotential with respect to the reduction of the dissolved HV^{2+}.

$$HV^{2+}{}_{ads} + 1e^- \rightleftarrows HV^{+}\cdot{}_{ads} \qquad (3.5)$$

Upon reduction, an ordered layer will rapidly form with adsorbed counterions from the electrolyte.

$$HV\cdot{}^{+}{}_{ads} + Br^-{}_{ads} \rightleftarrows HVBr_{ads} \qquad (3.6)$$

In this work, the applied potential was purposely kept sufficiently positive to avoid outer-sphere reduction of dissolved HV^{2+}. Instead, the voltammetric responses for the Hg macro- and microelectrodes were both diagnostic of what has been reported previously for reaction *3.5*. The only differences in the two responses were similar to what was described above, i.e. the peak widths were larger and the dependence of the peak current with scan rate was shallower with the macroscale Hg pool electrodes. Again, these observations are consistent with the fact that the much smaller currents at Hg ultramicroelectrodes are not subject to appreciable distortion from uncompensated resistance. The wave widths and the scan rate dependence of the peak currents were all in accord with models in which the electron transfer step is fast.[22]

3.4.3 Borate

The adsorption of borate species has been described previously on solid metal electrodes but never extensively investigated on Hg (or any other liquid metal electrode). On solid metal electrodes, the adsorption of borates is believed to follow from the dissociation of $B_4O_7^{2-}$ in solution (reaction *3.7*).[21,30] Condensation of boric acid and tetrahydroxyborate can form borate anions (reaction *3.7* and *3.8*).[21]

$$B_4O_7^{2-} + 7H_2O \rightleftarrows 2B(OH)_4^- + 2B(OH)_3 \qquad (3.7)$$

$$2B(OH)_3 + 2B(OH)_4^- \rightleftarrows B_3O_3(OH)_4^- + 3H_2O \qquad (3.8)$$

On solid electrodes, the adsorption of borate species occurs at the *pzc*, in accord with the adsorption arising only from an affinity between anions and a positively charged surface. For example, when the potential of the electrode is moved to a potential more positive than the *pzc*,

the net positive surface charge character facilitates adsorption of anions. The concentration dependence of the responses collected with the Hg ultramicroelectrode are consistent with polyborate species like $B_3O_3(OH)_4^-$ being the relevant anions (rather than borax, $B_4O_7^{2-}$) since reactions *3.6* and *3.7* favor the formation of $B_3O_3(OH)_4^-$ at higher concentrations of borax and the voltammetric features sharpened considerably with higher concentration, as has been observed previously at Ag electrodes.[21] However, the data collected here for Hg instead suggest adsorption is occurring in conjunction with Hg oxidation, similar to the adsorption of Br^-. Specifically, both Hg electrode types yielded voltammetric waves far from the *pzc* of Hg (-0.19 V vs. normal hydrogen electrode)[4] and instead closer to potentials where Hg can be electrochemically oxidized. Therefore, the more appropriate description for the surface film from these voltammetric experiments is described by reactions *3.9* and *3.10*.

$$Hg \rightleftarrows Hg^+_{ads} + 1e^- \qquad (3.9)$$

$$Hg^+ + B_3O_3(OH)_4^-{}_{ads} \rightleftarrows Hg\ B_3O_3(OH)_{4\ ads} \qquad (3.10)$$

For the bulk pool electrode, the voltammetry did not contain sharp features at any scan rate. This observation could imply either the layer is highly disordered and/or unstable, i.e. is not still on the electrode surface upon the negative potential sweep. Based on the responses observed with the Hg ultramicroelectrode, this latter possibility is likely. Specifically, the slow scan voltammetry with the Hg ultramicroelectrode also did not show a significant cathodic peak, implying that no surface layer was available to be reduced. However, the sharp and extremely prominent cathodic wave in the comparatively faster scan experiments implied that an

electroactive film was produced and reducible at short times. A plausible explanation is that the 'Hg-borate' surface film formed at positive potentials has some solubility in solution and dissolves into solution at some finite rate, resulting in a clean film. If the potential is swept much slower than this dissolution rate, then the film is essentially gone by the time the negative sweep begins. However, at faster scan rates, the potential sweep outpaces any chemical dissolution and the film can be reduced back to Hg^0 and adsorbed/desorbed $B_3O_3(OH)_4^-$. The odd observation of an anodic peak during the *cathodic* sweep at low scan rates with the Hg ultramicroelectrode further support this interpretation. That is, as the potential is swept more negative than the switching potential, an anodic current arises from the oxidation of Hg because the electrode surface is effectively 'clean' since the surface film has dissolved away.

Two confounding aspects complicate (but do not rule out) the interpretation of an unstable 'Hg-borate' film. First, it is presently unclear why the Hg borate film forms only in a narrow potential range at the ultramicroelectrode but not at the bulk pool electrode. The voltammetry at the bulk Hg pool electrode at potentials more positive than E = -0.1 V show no peak, implying that the oxidative current continues unabated. This fact may suggest that there is some complex interplay between mass transport, adsorption, and electrooxidation of Hg. That is, if Hg^+ complexes with the borate condensation products, then the feed rate of borates to the surface may control whether the product of Hg oxidation is a continuous film or an incomplete film. Presumably, if the mass transport of borate species to the surface is fast, as would be expected at an ultramicroelectrode operating under radial mass transport, Hg oxidation is limited by the fast, complete formation of a film that then slowly dissolves away. But if the mass transport of borate species is slow, as expected for a macroscopic electrode under the control of linear diffusional mass transport, then perhaps a surface film never saturates and the oxidation of

the Hg surface is never limited by film formation. Second, dissolution of a 'Hg-borate' film would necessarily imply etching of the Hg electrode. At the Hg ultramicroelectrode, this could be deleterious, as the amount of total Hg is finite. However, the multiple voltammetric sweeps indicate that the underlying Pt is never exposed at the ultramicroelectrode (e.g. no change in capacitance, no increased activity for H^+ reduction). Accordingly, at the ultramicroelectrode, the effective etch rate must be small and in accord with the removal of monolayers rather than substantial volumes.

3.5 Conclusion

The original premise of this work was to ascertain whether aspects such as electrocapillarity and mass transport deleteriously affect surface processes at small liquid metal electrodes. The cumulative data strongly suggest that electrocapillarity is not a mitigating factor. If it was, then more pronounced differences would have been observed in the voltammetry with Br^- and HV^{2+}. Since the converse was seen (i.e. identical qualitative features), the most probable conclusion is that mechanical perturbations are not of concern in surface-based processes such as ec-LLS at Hg microdroplet electrodes.

Regarding mass transport, the data do seem to support the notion that the relatively fast mass transport at small liquid metal microdroplets is influential to varying degrees. In processes involving Br^- and HV^{2+}, the principal effect was that the voltammetric features were undistorted at fast scan rates that are ordinarily inaccessible at macroelectrodes. In this regard, the work here suggests that microdroplet platforms may be potentially useful to study the 2D crystallization phenomenon in the formation of halide and viologen adlayers. For more chemically complex processes like the adsorption of borates, the transport of species to the electrode apparently

strongly influences the voltammetric response type and (accordingly) the presence of any surface layer. In this respect, the data suggest that a more comprehensive investigation of how the borate voltammetry changes with electrode size would be informative and perhaps the best way to decouple the interplay between the rates of the involved chemical and electrochemical steps.

Finally, an unintended but clear demonstration of this work is the utility of ultramicroelectrodes for the collection of 'clean' adsorptive voltammetric data. Specifically, '*iR*' distortion that broadens voltammetric waves and decrease the magnitude of peak currents do not hamper the raw data at small Hg ultramicroelectrodes and allow testing of established adsorption/desorption models.[22]

3.6 References

1. R. J. Forster, *Chem. Soc. Rev.*, **23**, 289 (1994).
2. J. Heinze, *Angew. Chem. Int. Ed.*, **32**, 1268 (1993).
3. C. G. Zoski, *Electroanalysis*, **14**, 1041 (2002).
4. D. C. Grahame, *Chem. Rev.*, **41**, 441 (1947).
5. C. B. Eaker and M. D. Dickey, *Appl. Phys. Rev.*, **3**, 031103 (2016).
6. M. Frieder and B. Jean-Christophe, *J. Phys.: Condens. Matter*, **17**, R705 (2005).
7. I. Morcos and H. Fischer, *J. Electroanal. Chem. Interfacial Electrochem.*, **17**, 7 (1968).
8. C. W. Kim, I.-H. Yeo and W.-K. Paik, *Electrochimica Acta*, **41**, 2829 (1996).
9. J. Keizer, P. A. Rock and S.-W. Lin, *J. Am. Chem. Soc.*, **101**, 5637 (1979).
10. J. Olson, C. Ursenbach, V. I. Birss and W. G. Laidlaw, *J. Phys. Chem.*, **93**, 8258 (1989).
11. J. Ni, C.-J. Zhong, S. J. Coldiron and M. D. Porter, *Anal. Chem.*, **73**, 103 (2001).
12. S.-Y. Tang, K. Khoshmanesh, V. Sivan, P. Petersen, A. P. O'Mullane, D. Abbott, A. Mitchell and K. Kalantar-zadeh, *Proc. Natl. Acad. Sci.*, **111**, 3304 (2014).
13. Y. Kwang-Seok, C. Il-Joo, B. Jong-Uk, K. Chang-Jin and Y. Euisik, *J. Microelectromech. Syst*, **11**, 454 (2002).
14. H. A. Laitinen and E. I. Onstott, *J. Am. Chem. Soc.*, **72**, 4565 (1950).
15. R. Payne, *J. Chem. Phys.*, **42**, 3371 (1965).
16. J. M. Parry and R. Parsons, *J. Electrochem. Soc.*, **113**, 992 (1966).
17. W. Jin and J. Peng, *J. Electroanal. Chem.*, **345**, 433 (1993).
18. A. S. Baranski and A. Moyana, *Langmuir*, **12**, 3295 (1996).
19. K. Manandhar and D. Pletcher, *Talanta*, **24**, 387 (1977).
20. M. Röefzaad, M. Jiang, V. Zamlynny and K. Wandelt, *J. Electroanal. Chem.*, **662**, 219 (2011).
21. K. J. Stevenson, D. W. Hatchett and H. S. White, *Langmuir*, **13**, 6824 (1997).
22. M. S. Maestre, R. Rodríguez-Amaro, E. Muñoz, J. J. Ruiz and L. Camacho, *J. Electroanal. Chem.*, **373**, 31 (1994).
23. L. M. Peter, J. D. Reid and B. R. Scharifker, *J. Electroanal. Chem. Interfacial Electrochem.*, **119**, 73 (1981).
24. S. Fletcher, C. S. Halliday, D. Gates, M. Westcott, T. Lwin and G. Nelson, *J. Electroanal. Chem. Interfacial Electrochem.*, **159**, 267 (1983).
25. E. H. Boult and H. R. Thirsk, *Trans. Faraday Soc.*, **50**, 404 (1954).
26. A. G. Anastopoulos and A. A. Papaderakis, *Russ. J. Electrochem.*, **50**, 70 (2014).
27. D. L. Perry, *Handbook of inorganic compounds*, p. xxvii, CRC Press/Taylor & Francis, Boca Raton (2011).
28. C. L. Bird and A. T. Kuhn, *Chem. Soc. Rev.*, **10**, 49 (1981).
29. F. Kitamura, T. Ohsaka and K. Tokuda, *J. Electroanal. Chem.*, **347**, 371 (1993).
30. K. J. Stevenson, X. Gao, D. W. Hatchett and H. S. White, *J. Electroanal. Chem.*, **447**, 43 (1998).

Chapter 4

Voltammetry of Dilute Solutions of Dissolved GeO_2 at Hg Ultramicroelectrodes

4.1 Introduction

The reduction of GeO_2 dissolved in water is a key step in the electrochemical liquid-liquid-solid (ec-LLS) process for crystalline Ge. The reduction necessarily involves multiple electron transfers and several bond scissions. To date, the efficiency of this electrochemical reaction has not been considered in detail. The data shown in Figure 2.3 in Chapter 2 suggest that this reaction may not be 100% efficient with respect to faradaic charge. More clarity in the first stages of ec-LLS should help inform on how to improve the crystal formation steps.

Studies of the electrochemical reduction of dissolved GeO_2 using macroscale Hg electrodes have been reported previously.[1-4] Only one redox wave is seen in the voltammetry for the $4e^-$ reduction of GeO_2 but the voltammetry of the oxidation of Ge^0 sometimes shows two distinct waves.[1,2,5] The agreed upon interpretation is that there is a difference in the oxidation of Ge^0 crystal and Ge^0 solvated in Hg (i.e. amalgamated Ge).[1,2,5,6]

In Chapter 2, we presented data that showed that an anodic peak was observed only at fast scan rates and this corresponded to the oxidation of solvated Ge^0. We posited that at fast scan rates, there was insufficient time to nucleate and grow a Ge crystal. However, the charge under this peak represented only a fraction of the Ge^0 atoms that were putatively produced on the

cathodic scan. This discrepancy was not resolved at the time and thus motivated the work in this chapter.

In this chapter, data are presented and discussed from experiments where hemispherical Hg microdroplet ultramicroelectrodes were used to gain insight into the electrochemical reduction of dilute solutions of GeO_2. A model is presented that attempts to resolve experimental observations in the voltammetry.

4.2 Experimental

4.2.1 Materials

Platinum (Pt) wire (99.95%, 25 μm diameter) was obtained from Alfa Aesar. GeO_2 (99.99%, Sigma-Aldrich), $Na_2B_4O_7$ (≥99.5%, Sigma-Aldrich), $CaCl_2$ (97%, Fluka), C_3H_6O (ACS grade, Fisher), $Hg(NO_3)_2$ (98%, Alfa Aesar), KNO_3 (99%, Acros Organics), HNO_3 (65% Fisher Scientific), Ar(g) (99.998%, Detroit Metro Welding), GeO_2 (99.99%, Sigma-Aldrich), and $Na_2B_4O_7$ (≥99.5%, Sigma-Aldrich) were used as received. Water (Barnstead Nanopure) with a resistivity > 18 MΩ cm was used throughout.

4.2.2 Electrode Preparation

Pt wire was glued onto a small piece of glass slide with cyanoacrylate (Bob Smith Industries), and attached to a variable autotransformer with a voltmeter to control the potential applied. The Pt wire was etched under 4 V in a 20 wt% $CaCl_2$, 1:1 (v/v) water-acetone solution for 30 seconds.[7] The etched Pt microwire was then sealed inside a glass capillary tube via heating with a nichrome heating coil.[8] The sealed end was subsequently filed with sandpaper to expose the Pt wire. Electrical contact to the Pt microwire was made by soldering a copper wire. A solution containing 0.01 M $Hg(NO_3)_2$, 0.1 M KNO_3, and 0.5% HNO_3 was first prepared,

purged with Ar(g) for 15 min to eliminate oxygen from the solution, and then kept under an Ar(g) blanket. Hg was then electrodeposited onto the Pt ultramicroelectrode immersed in this solution while biased at -0.1 V for 5 min.[9] The diameters of the Hg hemispherical ultramicroelectrodes were between 6 and 9 μm.

4.2.3 Electrochemical Methods

CH Instruments models 420a and 760c potentiostats, and three electrode cells were used throughout. All potentials are referenced to a mercury/mercurous sulfate ($E(Hg/Hg_2SO_4)$) reference electrode, and a Pt mesh was used as the counter electrode.

4.3 Results

4.3.1 Cyclic Voltammetry

In Figure 4.1, slow (0.01 V s^{-1}) and fast (10 V s^{-1}) scan voltammetric responses were recorded in an aqueous solution containing 0.1 M $Na_2B_4O_7$ and a 0.0005 M formal concentration of dissolved GeO_2. In Figure 4.1a, the slow scan began at -0.4 V and showed the first cathodic feature when swept out to E = -1.4 V that appeared to have the characteristic steady-state current for a microelectrode. The magnitude of this steady-state current implied a reduction process involving about 1 electron.[10] At more negative potentials, another plateau began at E = -1.8 V. This steady-state current was much larger and was mixed with a non-limiting current at more negative potentials. The exponentially increasing current likely reflected the evolution of H_2 at the electrode surface. The reverse scan showed that the anodic current crossed over the cathodic current at E = -2.0 V. A broad anodic peak began at E = -0.53 V. The ratio of the total anodic to total cathodic charge was 4.9.

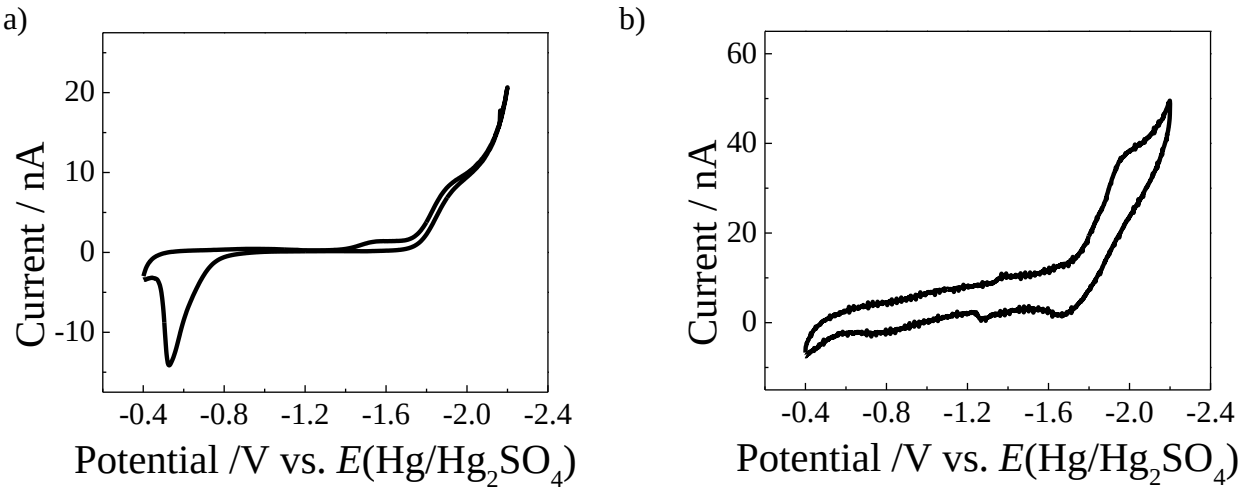

Figure 4.1 Voltammetric response of a Hg microdroplet ultramicroelectrode immersed in 0.1 M $Na_2B_4O_7$ and 0.0005 M GeO_2 at scan rates of a) 10 mV s^{-1} and b) 10 V s^{-1}.

In Figure 4.1b, the voltammetric response at 10 V s^{-1} was markedly different. Aside from the larger capacitive nature expected at faster scans, no steady-state currents were measured. Additionally, a slight peak was noted at ~ E = -1.9 V without appreciable contribution from H_2 evolution. On the reverse scan, there was signs of perhaps three anodic waves at E = -1.7, E = -1.3, and E = -0.8 V. The ratio of the total anodic to total cathodic charge was 0.06.

Figure 4.2 shows the same type of voltammetric data but in an electrolyte containing a 10x larger formal concentration of GeO_2 (0.005 M). At the slow scan rate in Figure 4.2a, again there was a cathodic feature with a steady-state current at E = -1.4 V. The magnitude of this steady-state current was about 10x larger than that in Figure 4.1a. This observation supports the possibility that this steady state current is due to the reduction of $HGeO_3^-$ to Ge^0, based on the standard potential for the redox couple.[11] The current was larger at increasingly more negative potentials, again with another current plateau at E = -1.6 V that was overtaken by H_2 evolution at even more negative potentials. The current on the anodic sweep also crossed over the cathodic current at E = -2.0 V. No anodic current was drawn until much more positive potentials, where a broader peak was seen as compared to Figure 4.1a. The ratio of the total anodic to total cathodic charge was 2.0.

Figure 4.2b shows the fast scan voltammetry for this solution. In this voltammetric response, a clear, single cathodic peak was observed at E = -2.0 V. The shape of this peak was broadly consistent with an irreversible redox process that becomes mass transport limited at more negative potentials. On the anodic sweep, no appreciable oxidative current passed until the most extreme positive potentials. Still, there was no sign of an apparent stripping peak. The ratio of the total anodic to total cathodic charge was 0.17.

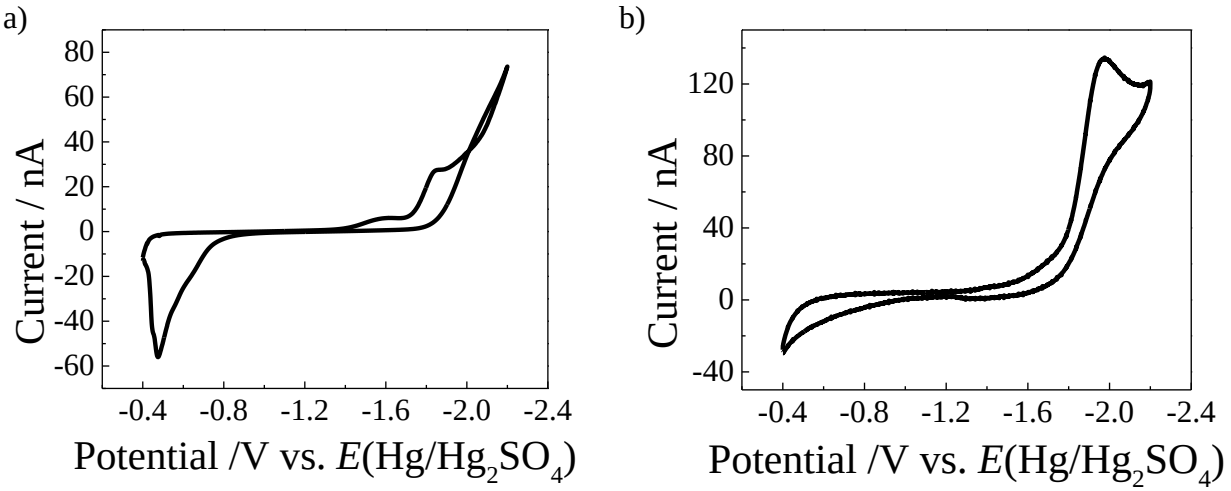

Figure 4.2 Voltammetric response of a Hg microdroplet ultramicroelectrode immersed in 0.1 M $Na_2B_4O_7$ and 0.005 M GeO_2 at scan rates of a) 10 mV s^{-1} and b) 10 V s^{-1}.

Figure 4.3 shows the slow and fast voltammetric responses in the same electrolyte but with a formal concentration of 0.025 M GeO_2. In Figure 4.3a, there was no identifiable current plateau at any potential. Instead, a prominent cathodic current at E = -1.75 V was noted that then was overtaken with current for H_2 evolution at more negative potentials. Again, the current on the anodic sweep did not match the recorded cathodic current. A cross-over between the two sweeps was apparent at E = -2.0 V. No further anodic current was passed until ~ E = -0.8 V, where a broad anodic wave began. This feature was much more asymmetric than either peaks in Figures 4.1a or 4.2a. The ratio of the total anodic to total cathodic charge was 1.8.

The fast scan voltammetry in Figure 4.3b again showed a current peak that was consistent with voltammetry that changed from kinetic to diffusion-limited current fluxes. The unique feature in the voltammetry in this electrolyte was the observation of a new symmetric anodic peak at E = -0.7 V. This peak is consistent with the oxidation of amalgamated Ge^0, i.e. Ge that is solvated within the Hg.[1,2] The ratio of the total anodic to total cathodic charge was 0.33.

To determine whether the oxidation of amalgamated Ge was observable at other concentrations with more persistent cycling, separate experiments were performed in solutions containing GeO_2 formal concentrations of 0.0005, 0.005, 0.010, and 0.050 M. Figure 4.4 shows experiments where the electrode was cycled between E = -0.4 and E = -2.2 V 20 times at a scan rate of 10 V s^{-1}. The 1^{st} and 20^{th} scan is shown in each plot. At every concentration, the voltammetric responses for the 1^{st} and 20^{th} scans were nominally similar but *not* identical. Specifically, the cathodic wave shape was more diffusive at the 20^{th} cycle (i.e. the curve after the peak showed a diffusion-limited decay shape) at formal concentrations of 0.005 and 0.010 M. This peak current increases linearly with concentration of dissolved GeO_2, in accordance with the Randles-Sevcik relation.[12] For every plot in Figure 4.4, the anodic sweep at the 20^{th} cycle had

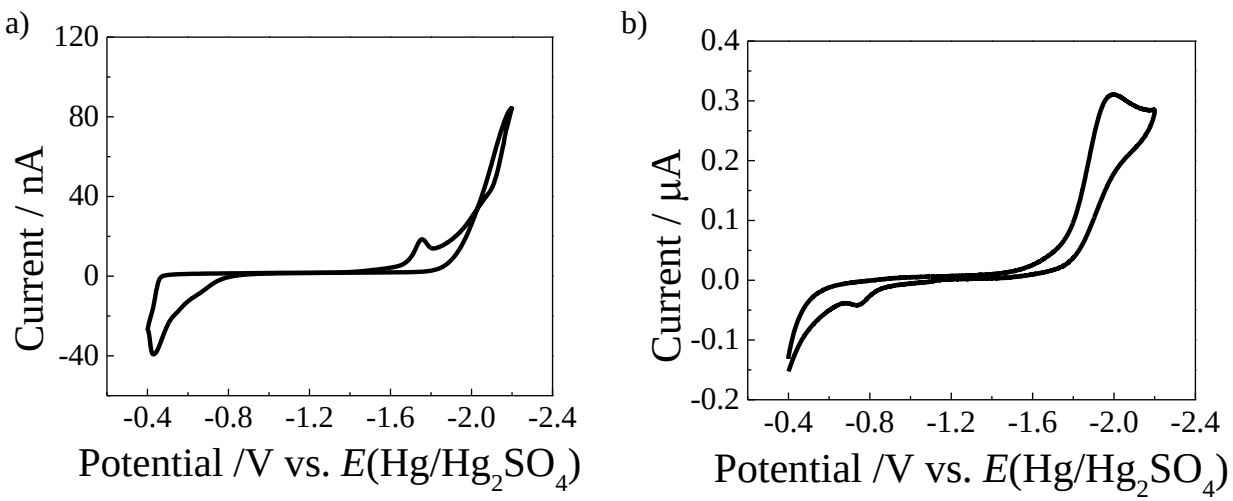

Figure 4.3 Voltammetric response of a Hg microdroplet ultramicroelectrode immersed in 0.1 M $Na_2B_4O_7$ and 0.025 M GeO_2 at scan rates of a) 10 mV s^{-1} and b) 10 V s^{-1}.

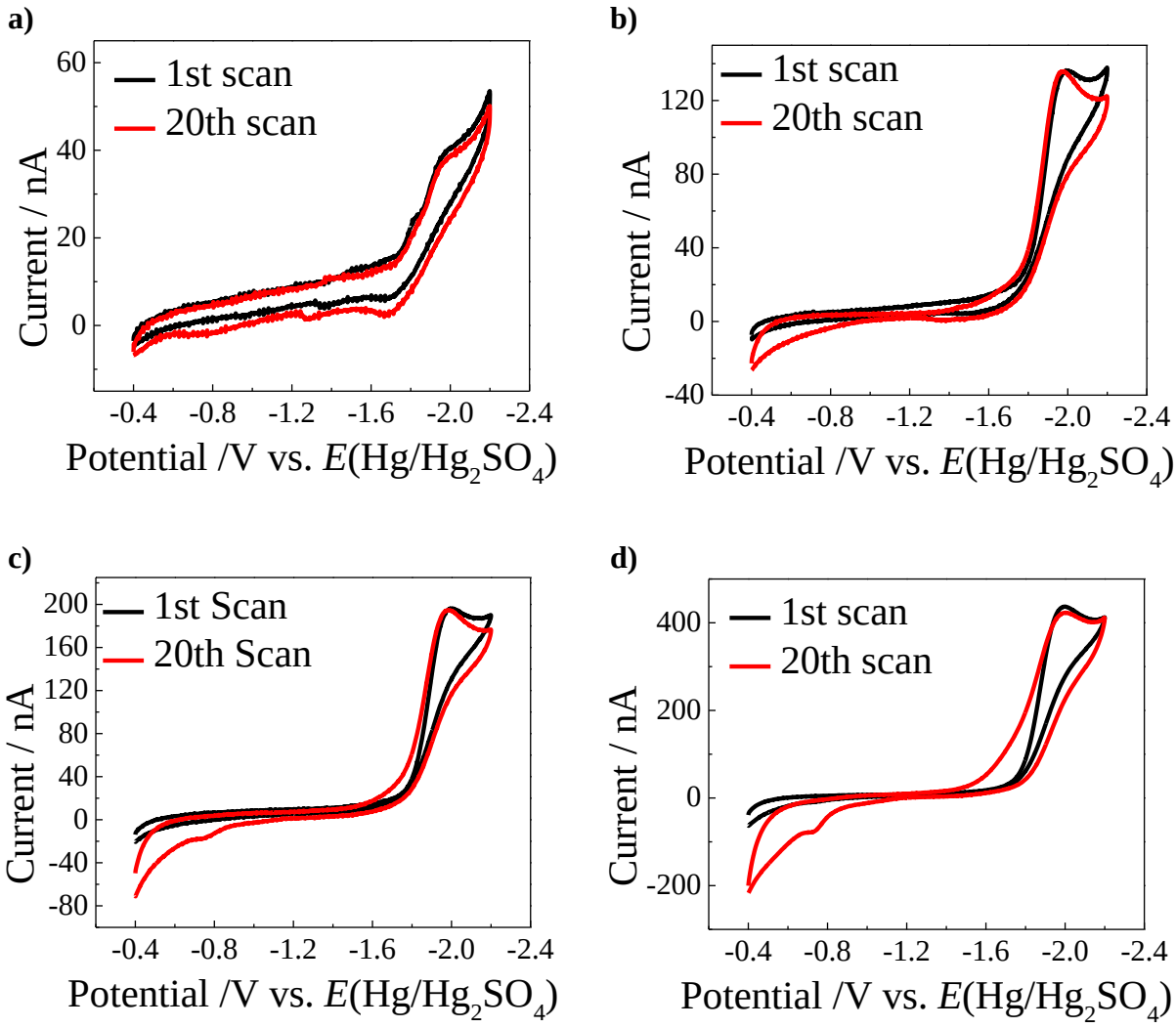

Figure 4.4 Voltammetric responses at select scan cycles of a Hg microdroplet ultramicroelectrode immersed in 0.1 M $Na_2B_4O_7$ and a) 0.0005 M GeO_2, b) 0.005 M GeO_2, c) 0.010 M GeO_2 and d) 0.050 M GeO_2 at a scan rate of 10 V s^{-1}.

more anodic current at potentials more positive than E = -0.8 V. However, only voltammetric responses in solutions with formal GeO_2 concentrations of > 0.005 M showed an oxidative stripping wave for the oxidation of amalgamated Ge.

4.4 Discussion

The presented voltammetry data suggest two new aspects regarding Ge ec-LLS at Hg electrodes. First, in Hg microdroplets, there is a complicated interplay between the rates of electroreduction, Ge dissolution, and Ge nucleation/crystallization. Second, the data suggest that the electroreduction of GeO_2 is not efficient in terms of faradaic charge or conservation of Ge.

Figure 4.5 shows a schematic illustration of the relative processes involved at these Hg ultramicroelectrodes during the voltammetric studies of GeO_2. Each arrow denotes a process with a characteristic rate. The cathodic current, $i_{cathodic}$, represents literally the rate of Ge^0 introduced to the surface of the Hg. If proper corrections are made for the faradaic efficiency of the GeO_2 reduction process, this rate is precisely known. The rate of dissolution of Ge^0 into Hg is unknown but if we consider it to be sufficiently fast (i.e. instantaneous), then the rate of transport of Ge^0 into the interior of Hg is the next potentially limiting process. This rate is governed by the diffusion of Ge^0 in Hg. At T = 25 °C, the diffusion coefficient for Ge in Hg is 1.3 x 10^{-5} cm^2 s^{-1}.[1] In a hemispherical drop with a diameter of 9 μm, the total time needed to diffuse from the surface to the center is 0.008 s. This time represents the upper limit on residence time of Ge in Hg, as a solvated Ge atom may only need to diffuse a shorter distance to undergo nucleation and crystallization. The rates of nucleation and crystallization (k_{nuc} and k_{cryst}) cannot be separated in this work. However, previous experiments from our group suggest that k_{nuc} is the slower step in ec-LLS[13] and that they have to occur serially in order for a crystal to form. Accordingly, the rates

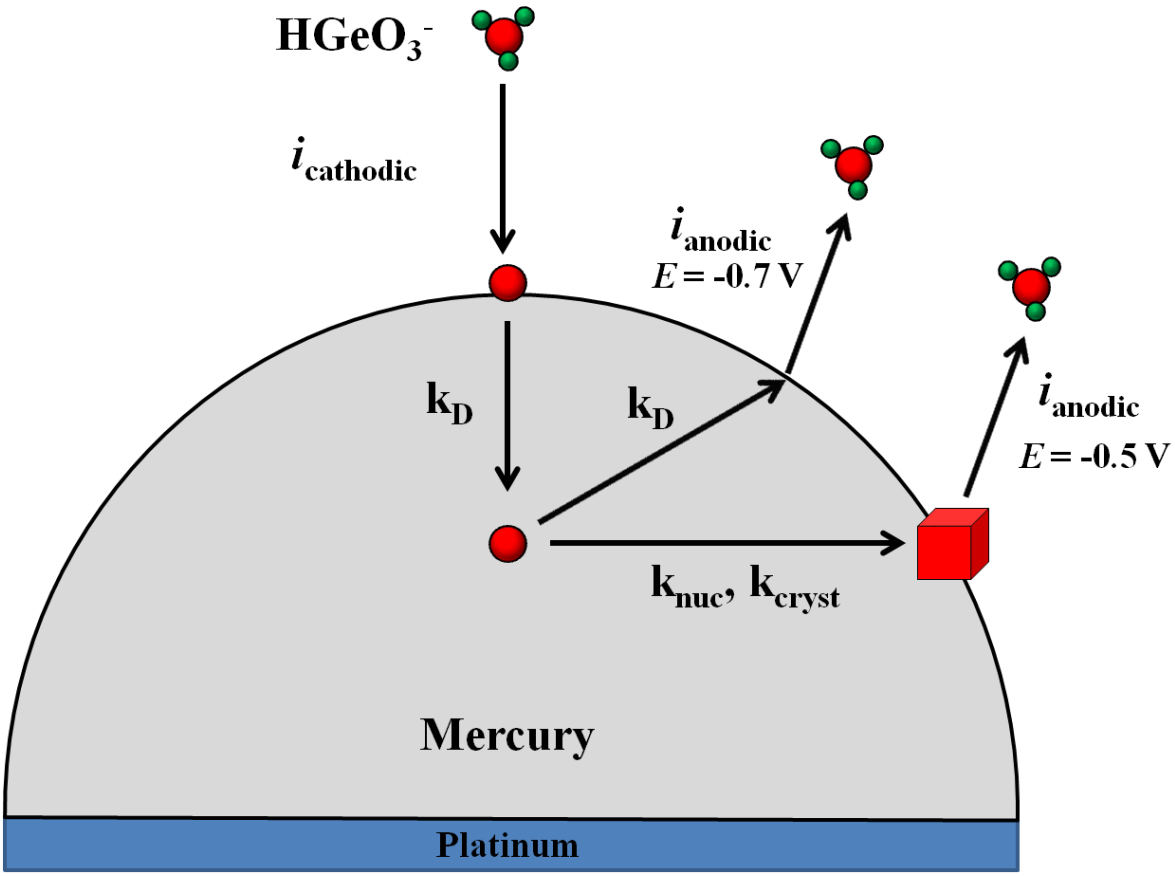

Figure 4.5 Schematic of the redox processes at Hg microdroplet ultramicroelectrodes during cyclic voltammetry with dissolved GeO_2. $i_{cathodic}$ represents the rate of Ge introduction onto Hg, k_D is the rate of diffusion of Ge in Hg, k_{nuc} is the rate of nucleation, k_{cryst} is the rate of crystallization, $i_{anodic,\ E=-0.7\ V}$ represents the rate of oxidation of amalgamated Ge^0 and $i_{anodic,\ E=-0.4\ V}$ represents the rate of oxidation of crystallized Ge^0.

of the two processes do not need to be distinguished but collectively they define how long it takes for a Ge crystallite to form. The oxidation of either amalgamated Ge^0 or crystallized Ge^0 are again known precisely from the anodic currents measured at the two anodic waves shown in this work ($i_{anodic,\ E=-0.7\ V}$ and $i_{anodic,\ E=-0.4\ V}$, respectively).

This model, in conjunction with certain facts regarding the relevant heterogeneous electron transfer processes, is sufficient to rationalize the observations in the presented voltammetry. The first relevant electrochemistry fact is that the heterogeneous reduction of H^+ to H_2 in water is significantly faster at solid Ge surfaces as compared to liquid Hg surfaces. The relevant exchange current densities for the H^+/H_2 couple at these two electrode types are 10^{-6} to 10^{-9} and 10^{-13} A cm^{-2}, respectively.[14,15] Second, the electroreduction of dissolved GeO_2 (i.e. $HGeO_3^-$ in these electrolytes) cannot proceed on solid electrode interfaces.[16-18] On solid electrodes, the electroreduction of $HGeO_3^-$ self-passivates after the deposition of 1-4 monolayers.[19] On a liquid metal electrode, the reaction proceeds unabated. The origin(s) of this disparity are not fully known, but nevertheless results in striking selectivity for this reaction when liquid metals are used. That is, no appreciable current can be ascribed to the reduction of $HGeO_3^-$ on Ge, even after Ge crystallites form on a liquid metal surface. Accordingly, we interpret the voltammetric responses as follows.

In Figures 4.1a, 4.2a and 4.3a, the voltammetry are consistent with an accumulation of Ge^0 occurring at the surface rapidly, as the currents for H_2 evolution didn't match in the cathodic and anodic sweeps. The lack of an anodic peak for the oxidation of amalgamated Hg^0 suggests that Ge nucleation & crystal growth occurred and depleted the Hg of any amalgamated Ge during the time the electrode was first moved negative enough to reduce $HGeO_3^-$ and then positive enough to oxidize Ge^0. The time to scan from -1.8 V to -2.2 V and then back to -0.8 V

(180 s) was sufficiently long that crystallization and nucleation occurred so as to eliminate any stripping wave indicative of amalgamated Ge^0. The loss of a steady-state character and more pronounced peak shape at higher dissolved GeO_2 concentrations does not imply a transition from radial to linear diffusion for the reduction of dissolved GeO_2. Instead, the cathodic 'peaks' in Figures 4.2a and 4.3a are consistent with the electrode surface switching from Hg to Ge character, with the latter being inactive for reduction of dissolved GeO_2. The reason for the progressively more distorted anodic wave shape for crystalline Ge^0 oxidation between Figures 4.1a, 4.2a, and 4.3a is not clear but could result from greater *iR* loss across thicker amounts of crystalline Ge.

The model in Figure 4.5 also helps rationalize the presented fast scan voltammetry. Apparently, the time to scan from -1.8 V to -2.2 V and then back to -0.8 V is sufficiently short at 10 V s^{-1} (0.18 s) that the oxidation of amalgamated Ge is observable (Figures 4.3b, 4.4c) when the concentration of dissolved GeO_2 is $\geq$ 0.01 M. This fact, in conjunction with an absence of the oxidation wave for crystalline Ge at these fast scan rates, suggests that the rate of Ge nucleation & crystal growth in Hg is not instantaneous but instead perhaps on the order of 10^{-1} s or slower. An alternative interpretation is that the amount of Ge^0 introduced in each cathodic sweep in the fast voltammograms is insufficient to saturate the Hg droplet. If all the cathodic charge in the fast scan voltammetry of 0.05 M GeO_2 arose from the formation of Ge^0, then the upper limit for the concentration of Ge in Hg would be 0.03 M (4.7×10^{-4} mol%), a value much greater than the thermodynamic solubility limit (3×10^{-7} mol%).[20] The fact that Ge could be accumulated over repetitive scans is indicated in the voltammetry in Figure 4.4, where the anodic wave for the amalgamated Ge was not visible in the first scan, where the concentration of Ge dissolved in Hg

was initially zero. In this viewpoint, the faradaic efficiency for formation of Ge^0 that can eventually be incorporated into a crystal is low.

Since the total cathodic charge is greater than the anodic charge at all GeO_2 concentrations at the fast scan rate, there are likely other reactions or processes that are operative. One possibility is the production of GeH_4 at extremely negative potentials. At alkaline pH, $HGeO_3^-$ is reduced to Ge, which can be further reduced to GeH_4.[21] The faradaic efficiency for the production of GeH_4 is likely higher in more concentrated solutions of GeO_2, which argues against this process being the determinant factor in the presented voltammetry. The formation of GeH_4 is largely dependent on the presence of Ge at the electrode.[21,22] As GeO_2 concentration increases, the formation of Ge^0 at the Hg surface also increases, which in turn should lead to more GeH_4. However, the opposite relationship is observed in the voltammetry, with the ratio of the anodic charge to the cathodic charge at fast scan rates actually increasing with greater GeO_2 concentration, implying the charge contribution by nonfaradaic processes is lower relative to the reduction of $HGeO_3^-$ to Ge.

Another possibility is the partial reduction of dissolved GeO_2 to stable/metastable Ge(II) species. The first steady-state currents in figure 4.1a and 4.2a suggest this is possible. If a substantial fraction of the current goes to the formation of Ge(II) species that remain in the electrolyte and undergo further reaction (or transport away from the electrode) such that they cannot be further reduced, then the total cathodic charge would overestimate the amount of Ge^0 produced.

A final possibility not considered in the model shown in Figure 4.5 is the formation of a Hg-Ge compound that is redox inactive. The phase diagram does not predict the existence of such a material, but recent reports suggest that metastable liquid metal alloys with Si can be

observed by shallow angle X-ray reflectivity,[23,24] indicating the formation of some yet unknown phase of Ge-Hg is possible. Even if this scenario did occur, it seems unlikely that all the amalgamated Ge would/could be 'trapped' in this state. Accordingly, while the voltammetry seem clear that the atom efficiency for the production of Ge is initially low, the reasons why require further investigation.

4.5 Conclusion

In this work, dilute GeO_2 solutions were used to determine how the reduction of GeO_2 and the oxidation of Ge^0 at Hg microdroplets changed depending on the potential sweep speed. At slow scan rates such as 10 mV s^{-1}, there is enough time after the reduction of the GeO_2 precursor for all the dissolved Ge^0 in the Hg microdroplet to nucleate and crystallize into Ge crystals, leaving no solvated Ge^0 to oxidize. At fast scan rates such as 10 V s^{-1}, the time period is too short for Ge crystals to form, and the anodic peak for amalgamated Hg can be observed, but only after multiple scan cycles. This delay may indicate that nucleation and crystal growth or the Ge^0 dissolution into the liquid metal itself it slow. The discrepancy between the anodic and cathodic charges at high scan rates indicates other nonfaradaic processes that require further experiments to identify.

4.6 References

1. Z. J. Karpiński and Z. Kublik, *J. Electroanal. Chem. Interfacial Electrochem.*, **81**, 53 (1977).
2. Z. J. Karpiński and Z. Kublik, *J. Electroanal. Chem. Interfacial Electrochem.*, **106**, 47 (1980).
3. A. K. Das Gupta and C. K. N. Nair, *Anal. Chim. Acta*, **9**, 287 (1953).
4. A. M. Shafiqul Alam, O. Vittori and M. Porthault, *Anal. Chim. Acta*, **102**, 113 (1978).
5. R. Kalvoda and N. Konopik, *Anal. Chem.*, **244**, 30 (1969).
6. Z. J. Karpiński and Z. Kublik, *J. Electroanal. Chem. Interfacial Electrochem.*, **226**, 331 (1987).
7. L. Libioulle, Y. Houbion and J. M. Gilles, *Rev. Sci. Instrum.*, **66**, 97 (1995).
8. C. G. Zoski, *Electroanalysis*, **14**, 1041 (2002).
9. J. Mauzeroll, E. A. Hueske and A. J. Bard, *Anal. Chem.*, **75**, 3880 (2003).
10. A. J. Bard and L. R. Faulkner, *Electrochemical methods: fundamentals and applications*, p. 171, Wiley, New York (2001).
11. M. Pourbaix, *Atlas of electrochemical equilibria in aqueous solutions*, p. 644, National Association of Corrosion Engineers, Houston, Tex. (1974).
12. A. J. Bard and L. R. Faulkner, *Electrochemical methods: fundamentals and applications*, p. 236, Wiley, New York (2001).
13. J. DeMuth, E. Fahrenkrug and S. Maldonado, *Cryst. Growth Des.*, **16**, 7130 (2016).
14. D. T. Sawyer, A. Sobkowiak and J. L. Roberts, *Electrochemistry for chemists*, p. 207, Wiley, New York (1995).
15. V. R. Erdelyi and M. Green, *Nature*, **182**, 1592 (1958).
16. G. Szekely, *J. Electrochem. Soc.*, **98**, 318 (1951).
17. J. I. Hall and A. E. Koenig, *J. Electrochem. Soc.*, **65**, 215 (1934).
18. O. Collenberg and K. Sandved, *Z. Anorg. Allg. Chem.*, **229**, 146 (1936).
19. X. Liang, Y. G. Kim, D. K. Gebergziabiher and J. L. Stickney, *Langmuir*, **26**, 2877 (2010).
20. C. Gumiński, *J. Mater. Sci.*, **24**, 2661 (1989).
21. V. V. Turygin, A. P. Tomilov, M. Y. Berezkin and V. A. Fedorov, *Inorg. Mater.*, **46**, 1459 (2010).
22. V. V. Turygin, M. K. Smirnov, N. N. Shalashova, A. V. Khudenko, S. V. Nikolashin, V. A. Fedorov and A. P. Tomilov, *Inorg. Mater.*, **44**, 1081 (2008).
23. O. G. Shpyrko, R. Streitel, V. S. K. Balagurusamy, A. Y. Grigoriev, M. Deutsch, B. M. Ocko, M. Meron, B. Lin and P. S. Pershan, *Science*, **313**, 77 (2006).
24. O. G. Shpyrko, R. Streitel, V. S. K. Balagurusamy, A. Y. Grigoriev, M. Deutsch, B. M. Ocko, M. Meron, B. Lin and P. S. Pershan, *Phys. Rev. B: Condens. Matter Mater. Phys.*, **76**, 245436 (2007).

Chapter 5

Future Directions

5.1 Introduction

The primary emphasis of the preceding chapters was the use of glass-encapsulated, micron-sized Hg ultramicroelectrodes within the context of the electrochemical liquid-liquid-solid (ec-LLS) growth technique. However, the basic concepts of interest are not limited to this particular size regime, liquid metal type, or even ultramicroelectrode design. Accordingly, this chapter describes some efforts that were undertaken to broaden the scope of this line of research. Described herein are individual datasets encompassing the use of nano-sized Hg droplets for ec-LLS, attempts to fabricate ultramicroelectrodes consisting of gallium (Ga), and the development of ultramicroelectrode platforms based on pinholes in a dielectric film. These data are presented to inform the reader on preliminary observations and on suggestions for future work.

5.2 Hg Nanodroplet Ultramicroelectrodes

The data shown in Chapter 2 indicate clear differences arise in the ec-LLS process when the volume of the liquid metal is substantially decreased. However, those data report only on the micron scale. It is presently unclear how Ge ec-LLS proceeds in *nanodroplets* of Hg, particularly when the size of the Hg volume approaches the size of the Ge crystallite/nucleus. There is no existing body of information that provides a basis to form a detailed prediction *a priori*.

Experiments were performed to fill this knowledge gap. A single nanodroplet of Hg was difficult to produce, as the electrochemical etching and glass encapsulation method described in Chapter 2 is not precise enough to produce submicron diameter electrodes.[1,2] Instead, random arrays of Hg nanodroplets were electrodeposited on a silicon substrate through brief (<10 seconds) chronoamperometry. Figure 5.1 shows the results observed after an attempt of Ge ec-LLS with Hg nanodroplets with diameters of 700 nm to 1200 nm. Extensive analysis of the films after attempted Ge electrodeposition showed little evidence of any Ge deposition, if any. Out of 9 trials, only in two long (13 hours) experiments were protrusions observed coming out of the liquid metal nanodroplets. At shorter experiment times, the Hg nanodroplets never showed any evidence of supporting nucleation/crystallization of Ge. High vacuum scanning electron microscopy is not suitable for imaging Hg nanodroplets, as the liquid metal easily boils off. Future imaging should make use of low vacuum or environmental scanning electron microscopes.

In contrast, Ge electrodeposition at Ga nanodroplets has been shown to produce Ge nanowires readily at time scales of 1 hour.[3,4] The use of a Ag/AgCl reference electrode may have interfered with Ge electrodeposition through leakage of the reference electrode electrolyte. Hg is known to react with Cl at open circuit potential to form Hg_2Cl_2 that can only be reduced at anodic potentials.[5-7] Hg_2Cl_2 can easily cover the entire surface of a Hg nanodroplet. Despite no Cl signal from energy dispersive x-ray spectroscopy (EDS) measurement, a thin layer of Hg_2Cl_2 may still exist on the Hg nanodroplet surface, preventing GeO_2 reduction. Experiments with Hg/Hg_2SO_4 reference electrode were not performed.

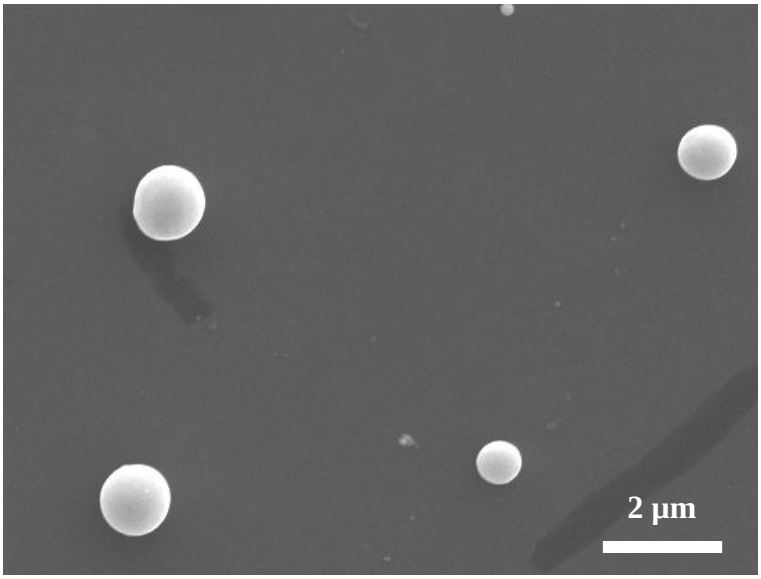

Figure 5.1 Top-down scanning electron micrograph of Hg nanodroplets on Si after electrodeposition at E = -1.4 V vs E(Ag/AgCl) for 20 min in a solution of 0.05 M GeO_2 and 0.01 M $Na_2B_4O_7$.

5.3 Ga Ultramicroelectrodes

For ec-LLS on the benchtop, the liquid metal used for the working electrode should have as low a melting point as possible. The two metallic elements that melt near ambient temperature are Hg and Ga. Both have been proven as viable medium for ec-LLS,[8] although Ga has shown some specific advantages. ec-LLS in Ga yields larger resultant crystallites.[9,10] The melting point of Ga is about 30°C, enabling comparisons between solid and liquid Ga.[11] The solubility of Ge in Ga is several orders of magnitude greater than the solubility of Ge in Hg (3×10^{-7} mol % in Hg vs 4.5×10^{-3} mol % in Ga).[12-14] A final practical advantage of Ga over Hg is the lower toxicity of Ga.[15-17]

A considerable effort was therefore focused on making Ga ultramicroelectrodes in the same manner as the Hg ultramicroelectrodes described in Chapters 2-4, with the replacement of a Ga (instead of Hg) electrodeposition step.[18] Cyclic voltammetry controls were run in the background electrolyte of 0.1 M KNO_3 with and without 0.1 M $Ga(NO_3)_3$ to determine a reliable potential at which the cathodic current with the Ga precursor was much higher than the background cathodic current (for H_2 evolution), as shown in Figure 5.2. Accordingly, an applied potential of E = -0.4 V vs Ag/AgCl was chosen for the chronoamperometric deposition of Ga on the Pt ultramicroelectrode. However, no deposits were seen by scanning electron microscopy after 5 minutes of electrodeposition time. Longer electrodeposition times and more negative applied potentials did result in some deposit (Figure 5.3) but it was not the expected hemispherical droplet of Ga. Instead, many small crystals on the Pt were observed, giving a grainy texture to the electrode. EDS measurement showed no Ge signal.

So as to eliminate any complications from electrodeposition, simple dipping of the Pt ultramicroelectrode directly into a bulk pool of liquid Ga was explored. Figure 5.4 shows some

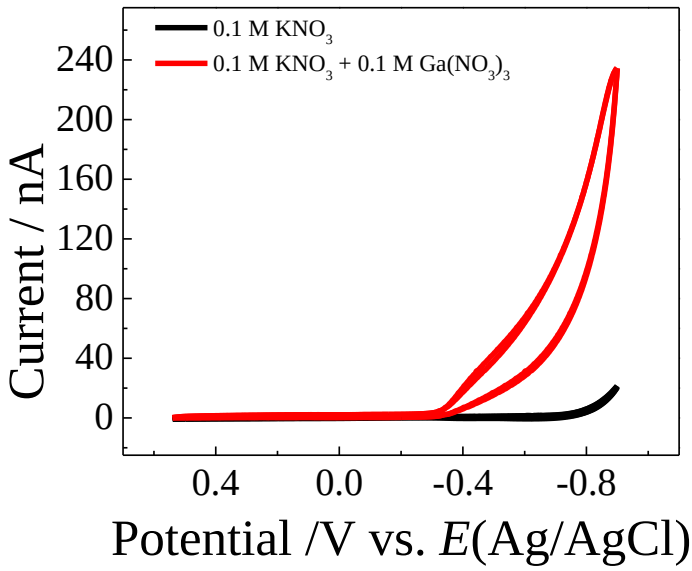

Figure 5.2 Comparison of the voltammetric responses of a Pt ultramicroelectrode immersed in 0.1 M KNO_3 with (red) and without (black) 0.1 M $Ga(NO_3)_3$. Scanning rate: 0.02 V s^{-1}.

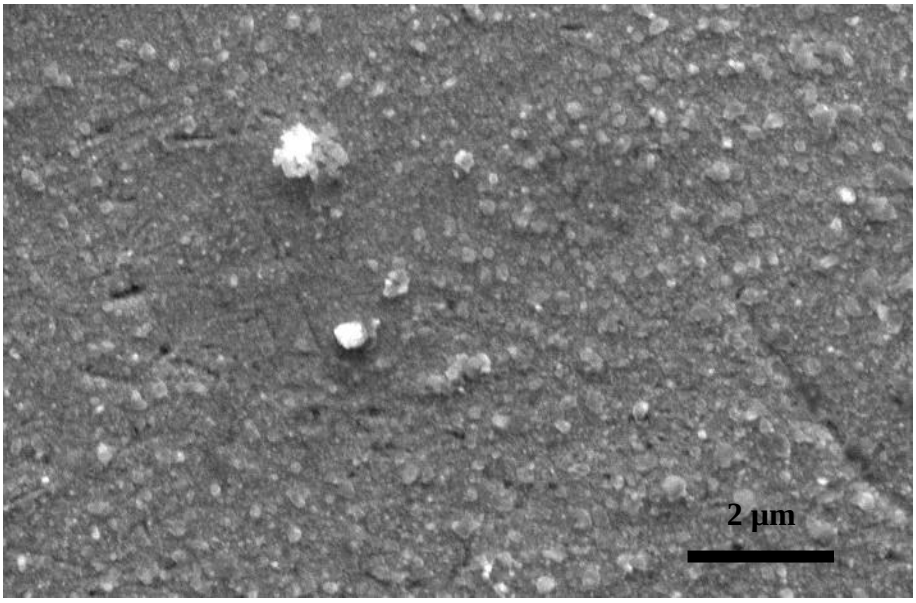

Figure 5.3 Scanning electron micrograph of Pt ultramicroelectrode after being immersed in a solution of 0.1 M $Ga(NO_3)_3$ and 0.1 M KNO_3 and biased at E = -0.7 V vs E(Ag/AgCl) for 15 hours.

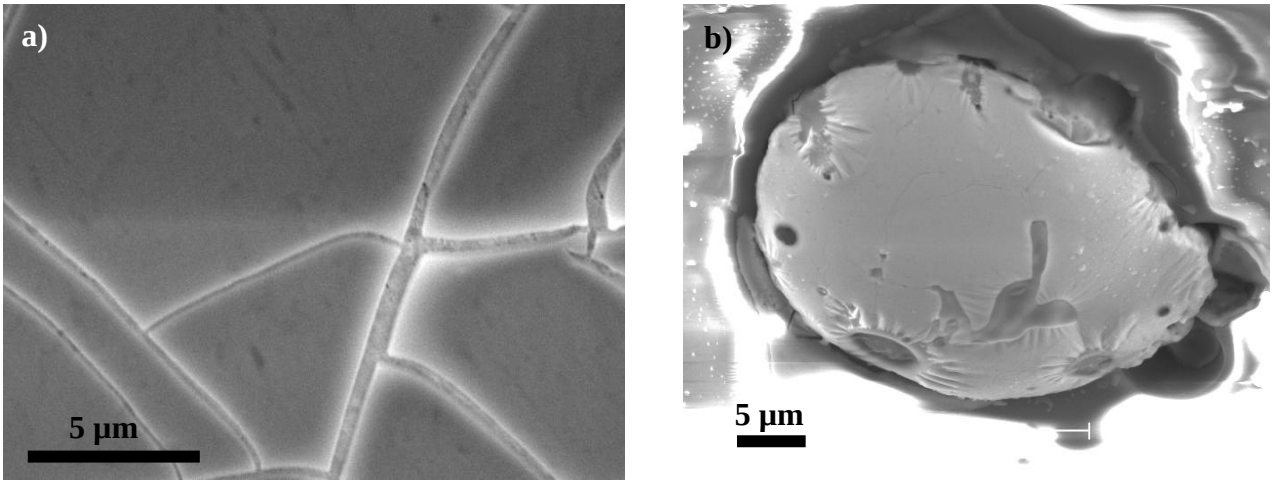

Figure 5.4 a) Scanning electron micrograph of a Pt ultramicroelectrode after dipping directly into bulk Ga pool. b) Scanning electron micrograph of a different Pt ultramicroelectrode after dipping directly into bulk Ga pool.

representative results. In Figure 5.4a, Ga was apparently deposited onto the Pt but not in the form of a spherical or hemispherical droplet. Instead, large, thin platelets were observed on the Pt surface, with continuous cracks between the platelets. EDS measurement in Figure 5.5 indicated the platelets consisted of Ga, Pt and Cl. The platelets were most likely not $GaCl_3$, as they remained even after immersion and washing with water, a solvent in which the compound is readily soluble.[19] The detected Cl was most likely from the HCl solution used to remove the oxide from the Ga pool for dipping. The platelets themselves were most likely the result of an alloying reaction between Pt and Ga.[20,21] The phase diagram of Ga and Pt, shown in Figure 5.6, suggest some solubility of Ga into Pt.[20] EDS measurements taken in the cracks between the platelets showed a strong Pt signal and a much weaker Ga signal. In a limited number of experiments, such as in Figure 5.4b, a rounded mass of Ga was observed, although the surface was always marked with small crystallites and never completely smooth. ec-LLS experiments performed with these platforms did yield some evidence of Ge microwire growth, but the results were inconsistent and formation of just a single microwire was never observed. After these trials, it was apparent that placing Ga directly on to a Pt ultramicroelectrode will not readily yield a microdroplet of Ga. Upon reflection, a complicating factor for Ga relative to Hg appears to be the large miscibility of Ga and Pt. Accordingly, additional refinements were explored.

Various buffer layers were placed on the Pt ultramicroelectrode to eliminate any alloying between Pt and Ga. Electrodeposition of In onto the Pt did not enable Ga electrodeposition. Alternatively, a layer of reduced graphene oxide is reduced onto the Pt ultramicroelectrode from a solution of graphene oxide and carbonate buffer[22] prior to Ga electrodeposition. In this case, the layer seemed to eliminate any Ga-Pt interaction but the electrodeposition consistently produced several sub-micron sized Ga droplets and not a single micron-sized droplet, as seen in

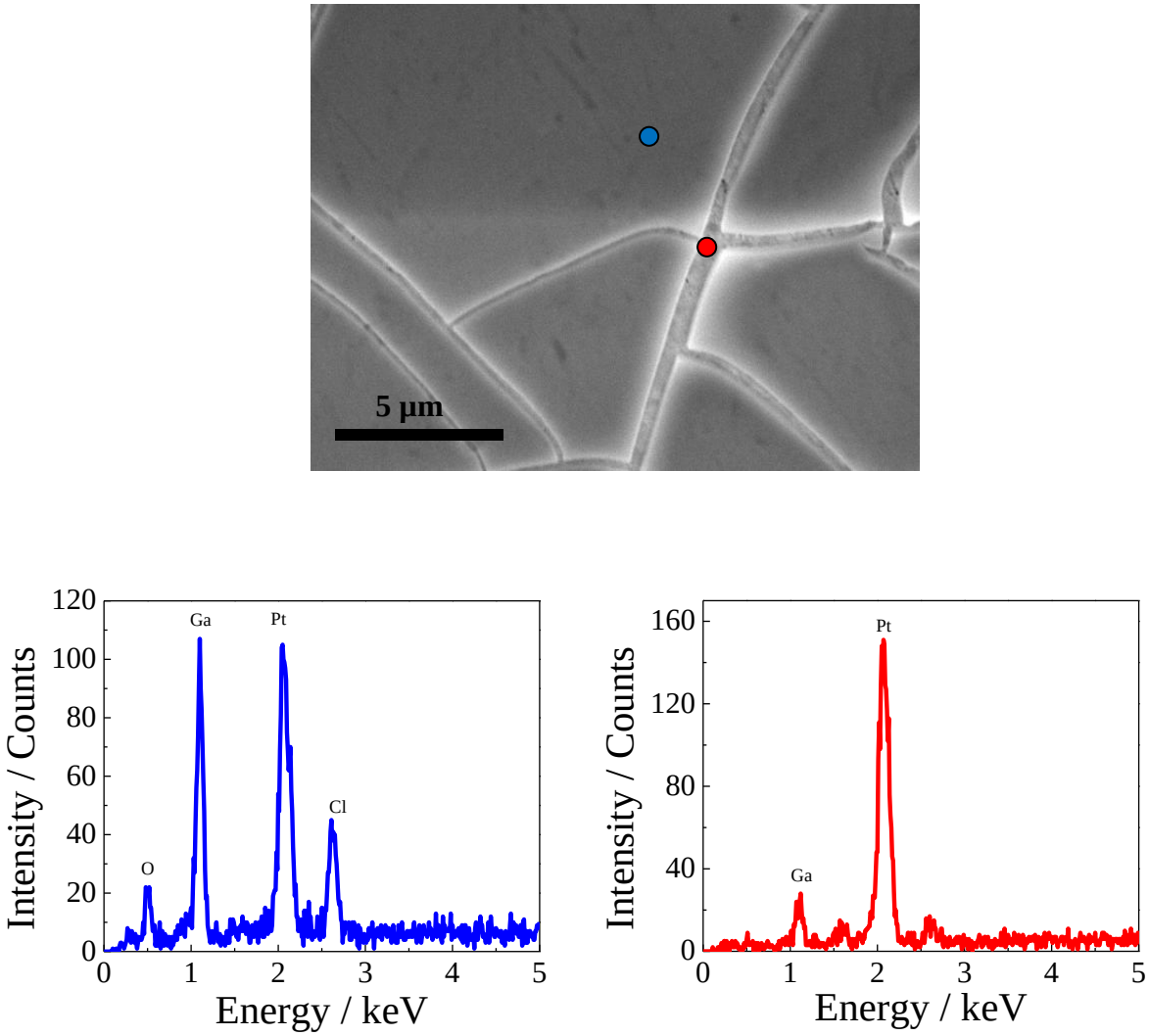

Figure 5.5 Energy dispersive X-ray spectra at two different points of a Pt ultramicroelectrode after dipping directly into bulk Ga pool.

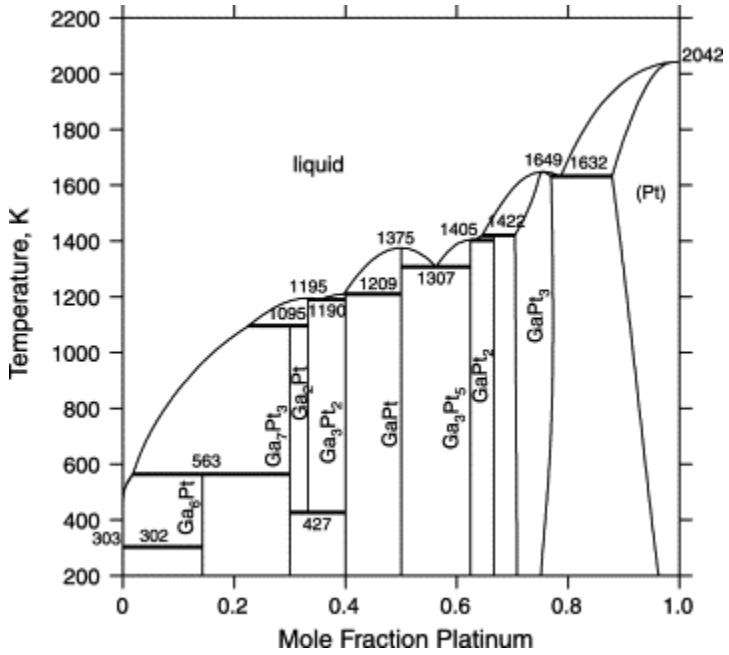

Figure 5.6 Binary phase diagram of Pt and Ga adapted from Reference 20.

Figure 5.7. Long electrodeposition times did not lead to coalescence, presumably indicating that a native oxide on the liquid metal droplets prevented fusion. An exhaustive attempt to promote coalescence was not performed and using the reduced graphene oxide layer in conjunction with physical dipping of the electrode into a Ga pool was not explored.

An alternative design comprised of a thin glass capillary filled with Ga but open on both ends was explored. In Figure 5.8, a Ga nanoelectrode made in this way is shown. These nanopipets were prepared and generously donated by the Baker Group at the University of Indiana. [23,24] The images show the platform both before and after cyclic voltammetry between E = -0.2 V and E = -2.0 V vs Ag/AgCl in an electrolyte of 0.01 M $Na_2B_4O_7$. Under these conditions, the Ga liquid is withdrawn from the tip of the capillary. Direct imaging of the process was possible but not performed. Nevertheless, the observations are consistent with the premise that upon applying a negative potential, the surface tension of Ga changes sufficiently to change the wetting of Ga, as electrocapillarity effects in liquid metals are known.[25,26] Scanning to E = -2.0 V vs Ag/AgCl also introduces H_2 evolution, which may have also played a part in pushing the Ga away from tip of the nanoelectrode. Several modifications may ameliorate this problem, including chemically modifying the interior glass surface of the capillary to make withdrawal of the Ga from the tip (and infiltration of water) more difficult, and limiting the applied potential to a range positive of H_2 evolution. Such methods were not explored.

Inadequate time was spent on further developing these methods to yield a ‘clean’ Ga ultramicroelectrode. Nevertheless, the conclusion from these efforts is that the preparation of a Ga ultramicroelectrode analogous to the Hg ultramicroelectrodes will inevitably be more involved. The Ga nanoelectrodes provided by the Baker Group can merit another attempt if movement of the liquid metal due to electrocapillarity can be limited through the insert of a solid

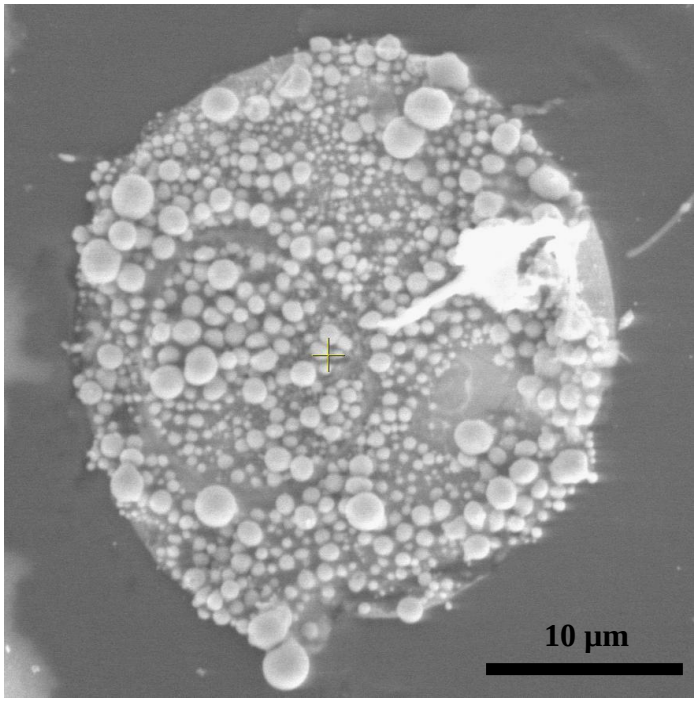

Figure 5.7 Scanning electron micrograph of Pt ultramicroelectrode with a reduced graphene oxide buffer layer after cyclic voltammetry to E = -1.4 V vs E(Ag/AgCl) in a solution of 0.1 $Ga(NO_3)_3$, 0.1 M KNO_3 and 0.1 M HNO_3.

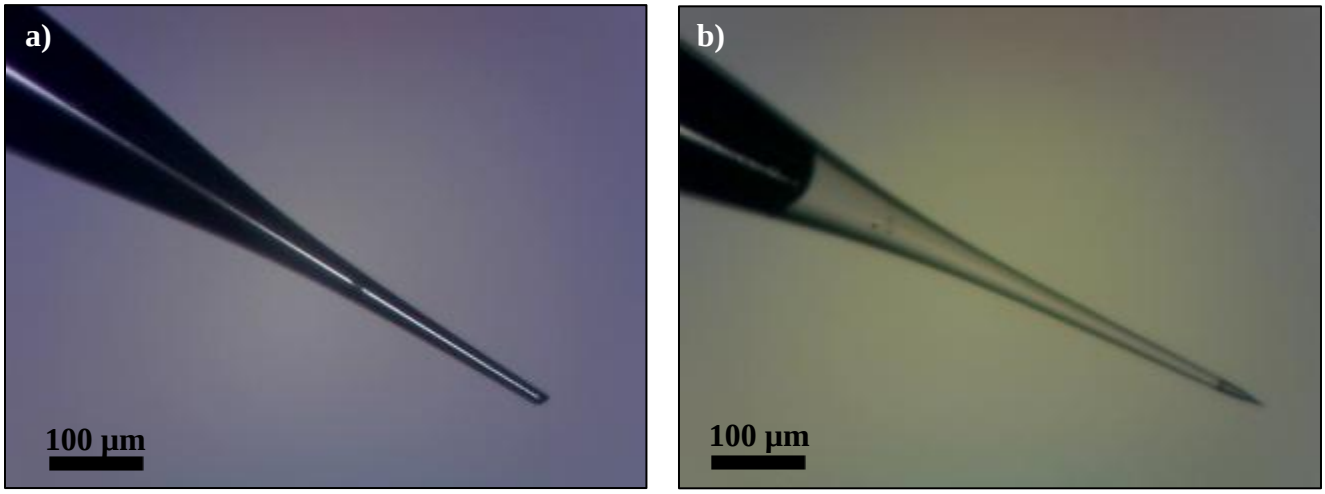

Figure 5.8 Optical microscope image of a Ga nanoelectrode a) before and b) after cyclic voltammetry in a 0.01 M $Na_2B_4O_7$ solution.

base to the non-tip end of the nanoelectrode. If the microelectrode platform approach is pursued, an electrode material such as carbon fiber may be more suitable to Ga electrodeposition, as it extends the potential window free of H_2 evolution. In a similar vein, a nonaqueous solvent could also be useful to limit H_2 evolution at more negative potentials. However, a different platform which does not necessitate electrodeposition of Ga at all can be a more fruitful direction, as is described in the following section.

5.4 Pinhole Ultramicroelectrodes

Two intrinsic flaws with the glass-embedded design for ultramicroelectrodes are the low throughput and high variability. The area of the Pt microdisk can vary in shape and diameter depending on the handling of the electrochemical etching, glass sealing, and polishing steps.[1,2] Even with the same electrodeposition conditions, the size of the Hg microdroplet can vary, indicating a faradaic efficiency less than 100%. Further, as mentioned above, the design is not readily amenable to other liquid metals.

An alternative ultramicroelectrode design can be adapted from the use of a flat, macroscale electrode coated with an insulating dielectric to make ultramicroelectrode arrays.[27-29] A simple means to this end is to pattern by photolithography just a single hole in a film of photoresist. The negative photoresist SU8 is a popular photoresist that is also a good dielectric.[30,31] If cast and patterned on a degenerately doped silicon substrate, then this type of ultramicroelectrode is readily obtained. Following either electrodeposition or the ‘smearing’ method popularized by Mr. Fahrenkrug in our lab,[32] liquid metal can then be easily introduced into these holes, forming a single microdroplet in electrical contact with the substrate on the bottom and with an electrolyte on top.

This method was used to prepare micron-sized liquid metal ultramicroelectrodes. Figure 5.9 shows optical and scanning electron images of the intentional pinhole in a film of SU-8 on a degenerately doped n-Si(100) substrate. These platforms were prepared by Mr. Fahrenkrug in the Kennedy group cleanroom facility. Cyclic voltammetric measurements in 0.001 M $Ru(NH_3)_6Cl_3$ and 0.1 M KCl with these pinhole ultramicroelectrodes exhibited the expected steady-state behavior, as shown in Figure 5.10. Since the mask used during photolithography ultimately defines the diameter of the pinhole, variation of the size and volume of the liquid metal volumes was possible. Pinhole diameters of 10, 20 and 30 μm were successfully used to make individual liquid metal ultramicroelectrodes.

Hg ultramicroelectrodes were prepared by electrodeposition into the pinholes. However, upon immersion and biasing these microelectrodes, the Hg was often lost. Corrosion was ruled out and again electrocapillary movement of the liquid metal could have caused the volume to be ejected from the pinhole. The confinement by the photoresist could focus the wetting forces on the liquid metal outwards. The loss of Hg was extensive for the smaller pinhole sizes. At a diameter of 30 μm, the Hg ultramicroelectrodes were stable enough to allow Ge ec-LLS. However, the results were consistently Ge films rather than any Ge microwire/nanowires, as shown in Figure 5.11. Insufficient repetitions were performed to determine if these results mirrored what is shown in Chapter 2 or if these Ge films had unique characteristics.

The pinhole ultramicroelectrode design was used for other liquid metals like the eutectic Ga-In. This specific liquid metal did not exit the photoresist pattern after use as an electrode and therefore allowed more facile repetition of ec-LLS experiments.

Figure 5.12 shows a Ge ec-LLS deposition on a Ga-In eutectic filled 20 μm diameter pinhole electrode immersed in a solution of 0.05 M GeO_2 and 0.01 M $Na_2B_4O_7$ and biased at E =

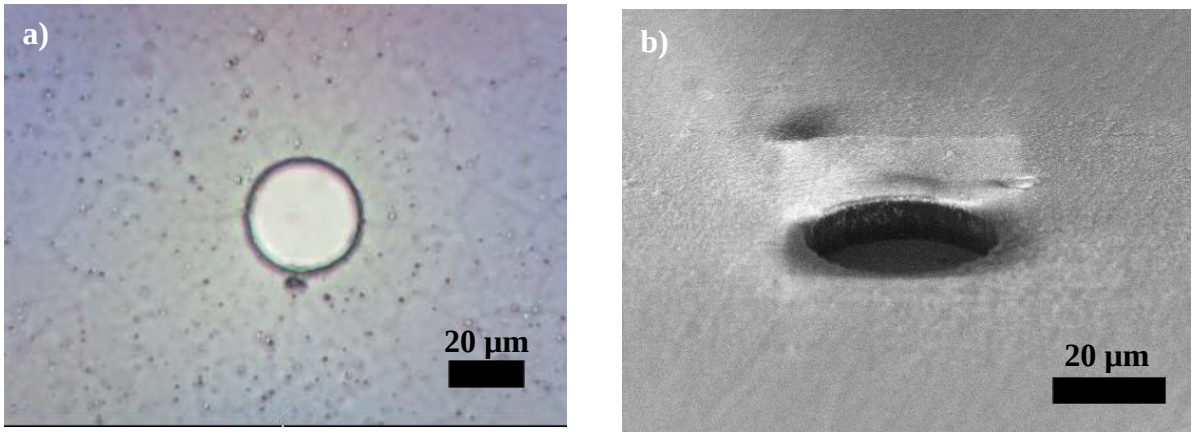

Figure 5.9 a) Optical image and b) scanning electron image of 30 µm diameter pinhole SU-8 pattern.

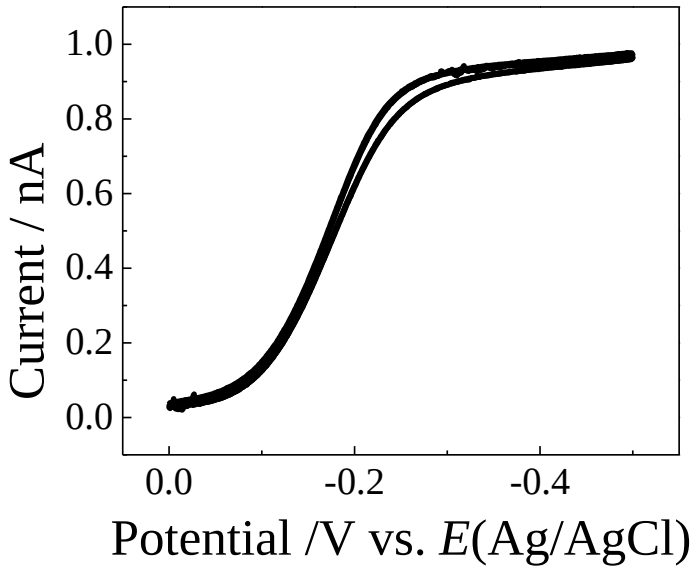

Figure 5.10 Steady-state voltammetric response of a 30 µm diameter pinhole electrode immersed in 0.001 M $Ru(NH_3)_6Cl_3$ and 0.1 M KCl. Scan rate: 0.02 V s^{-1}.

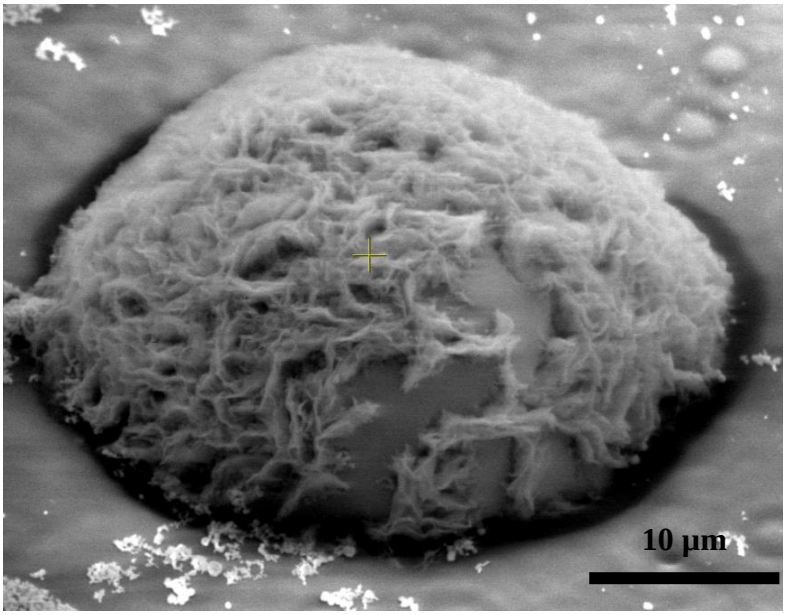

Figure 5.11 Scanning electron micrograph of a Hg-filled 30 µm diameter pinhole electrode after immersion in a solution of 0.05 M GeO_2 and 0.01 M $Na_2B_4O_7$ and biased at E = -1.4 V vs E(Hg/Hg_2SO_4) for 30 min.

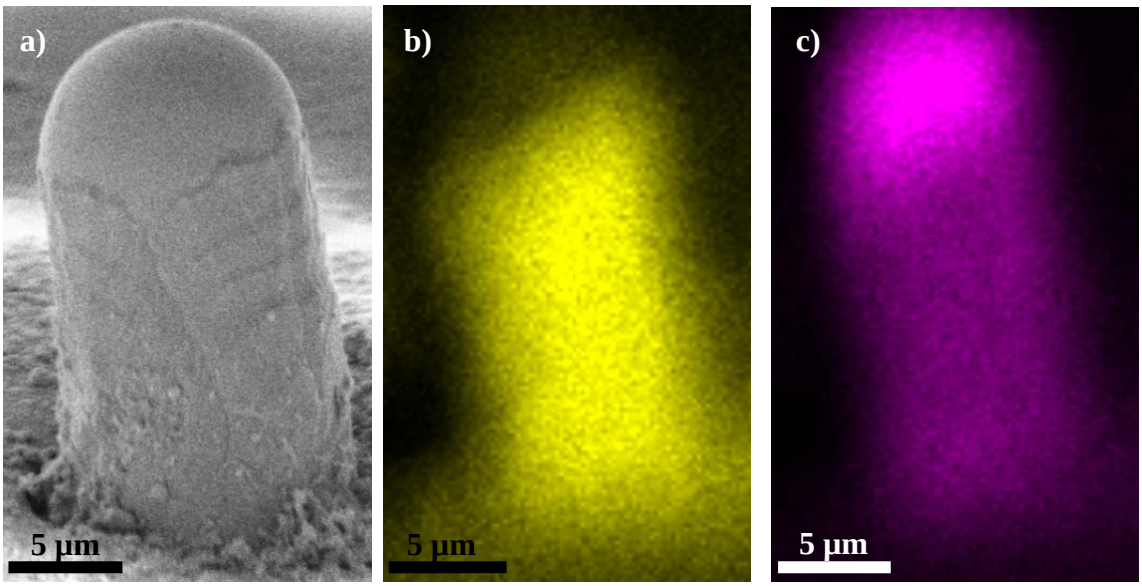

Figure 5.12 a) Scanning electron micrograph a Ga-In eutectic filled 20 µm diameter pinhole electrode after immersion in a solution of 0.05 M GeO_2 and 0.01 M $Na_2B_4O_7$ and bias at E = -1.6 V vs Ag/AgCl for 10 minutes surrounded by a 40°C bath. EDS mapping of the Ge microwire showing b) Ge and c) Ga.

-1.6 V vs Ag/AgCl for 10 minutes surrounded by a 40°C bath. In this case, the result of ec-LLS was an individual Ge microwire, as shown by the scanning electron image in Figure 5.12a. A liquid metal cap was observed at the top of each grown microwire. EDS measurements in Figure 5.12b and 5.12c indicated that the body of the microwire contains both Ge and Ga, with the Ga appearing homogeneously throughout. With larger pinhole diameters, smaller Ge nanowires were seen growing around the main microwire, indicating incomplete filling of the pinhole with liquid metal.

Preliminary experiments highlighted lack of a strong correlation between the measured current transient during ec-LLS and the morphology of the resultant Ge microwire, as shown in Figure 5.13. Despite nominally similar length/diameter, the two chronoamperometric data sets appear quite different. Faradaic current from hydrogen gas evolution operating in parallel further complicated interpretation of the transients. Specifically, the fraction of current for H^+ reduction should increase as the Ge microwire grows, as Ge is more active towards this redox process than bare eutectic Ga-In.[33,34]

To circumvent this problem, preliminary experiments were performed with Ga/In eutectic ultramicroelectrode arrays in propylene carbonate containing tetrabutylammonium iodide or tetrabutylammonium chloride as the supporting electrolyte and dissolved GeI_4 as the Ge precursor at 80°C. Though it has been observed that the growth of Ge microwires under these conditions with tetrabutylammonium chloride as the supporting electrolyte is possible, the results were inconsistent. Controls were conducted to rule out the photoresist itself being the problem and to confirm that the Ga-In eutectic was properly making contact with the Si substrate at the bottom of the holes. A common result observed was the lack of any Ge deposit, with the apparent loss of some of Ga/In eutectic in holes post-deposition, as the liquid metal is merely

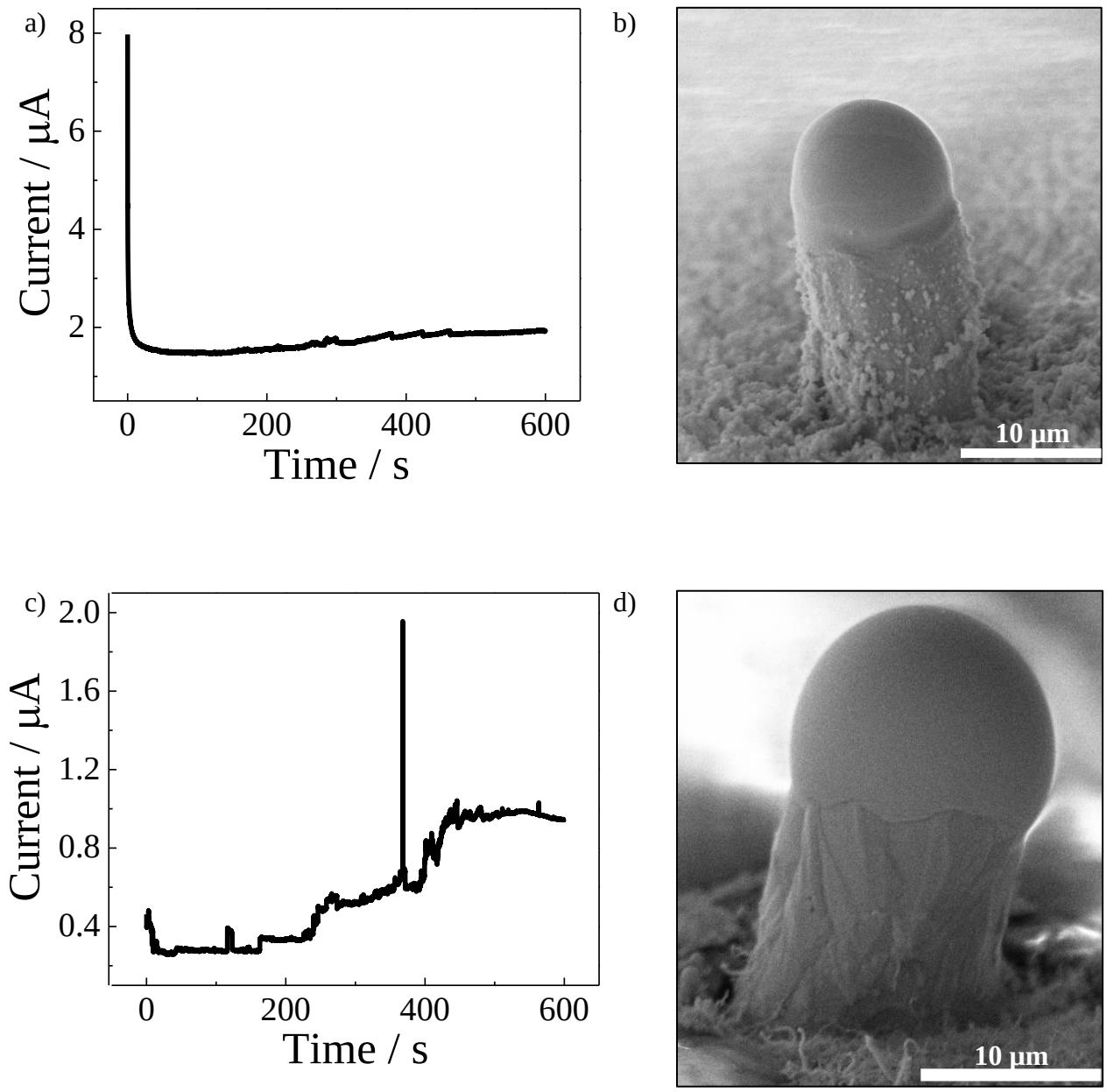

Figure 5.13 a) Current-time transient response for a Ga-In eutectic filled 20 μm diameter pinhole electrode after immersion in a solution of 0.05 M GeO_2 and 0.01 M $Na_2B_4O_7$ and bias at E = -1.4 V vs Ag/AgCl for 10 minutes surrounded by a 65°C bath. b) Scanning electron micrograph of a Ga-In eutectic filled 20 μm diameter pinhole electrode after the experiment shown in a). c) Current-time transient response for a different Ga-In eutectic filled 20 μm diameter pinhole electrode in the same conditions described in a). d) Scanning electron micrograph of a Ga-In eutectic filled 20 μm diameter pinhole electrode after the experiment shown in c).

level with the photoresist layer instead of forming a microdroplet above it. Ge crusts on the liquid metal were also seen. Extrusions resembling Ge microwires were sometimes observed, but parts of the structure appear to be lost after scanning electron imaging, leading to the conclusion that extrusions are likely non-crystalline and not true Ge microwires. Variations in the potential applied and the temperature bath were tested, but the results remained similar.

The pinhole platform lends itself well to systematic variation of a number of electrodeposition conditions for a single, individual microwire free from the influence of other neighboring growths. Different liquid metal mixtures can be applied to the pinhole. Variation in the hole diameter can reveal where the transition between microsize and macrosize morphology occurs. The shape of the hole can be easily changed, allowing study of crystallization and growth in nonstandard electrode shapes. The growth of single microwire from the pinhole platform in a clear electrochemical cell could be recorded with a high speed camera under a long distance optical microscope and paired with the corresponding current-time transient to have an even more direct visual correlation between the growth process and the electrochemical data.

5.5 Summary Prospective

While amenable for Hg microdroplets, the tactic of electrodepositing any desired liquid metal onto an existing, glass-encapsulated Pt ultramicroelectrode platform is difficult and not amenable for facile study of ec-LLS processes. The strategy of coating Pt to prevent liquid metal alloying appeared promising, particularly with the reduced graphene oxide films. The data suggest that this route may work better for nanoelectrodes but that requires further validation. Nevertheless, there are still several fertile areas of investigation involving liquid metal ultramicroelectrodes. The data shown here prove that Hg nanodroplets can be readily prepared

and incorporated into an ec-LLS scheme. Subsequent materials characterization is needed to identify why Ge crystals were not observed. This sort of work is readily doable and would serve as a good entry point for a 1st year graduate student. Finally, the pinhole platform is easily realized with Ga-based metals. It is not clear if Ga is required and effort should be spent using the pinhole ultramicroelectrode platform for other liquid metals. If successful, it should rapidly inform on whether the Ge microwires (and the electrochemical data collected during ec-LLS) are sensitive to the liquid metal.

5.6 References

1. L. Libioulle, Y. Houbion and J. M. Gilles, *Rev. Sci. Instrum.*, **66**, 97 (1995).
2. C. G. Zoski, *Electroanalysis*, **14**, 1041 (2002).
3. E. Fahrenkrug, J. Gu, S. Jeon, P. A. Veneman, R. S. Goldman and S. Maldonado, *Nano Lett.*, **14**, 847 (2014).
4. L. Ma, J. Gu, E. Fahrenkrug and S. Maldonado, *J. Electrochem. Soc.*, **161**, D3044 (2014).
5. M. A. Nolan and S. P. Kounaves, *Electroanalysis*, **12**, 96 (2000).
6. D. Jagner, E. Sahlin and L. Renman, *Anal. Chem.*, **68**, 1616 (1996).
7. N. F. Zakharchuk and K. Z. Brainina, *Electroanalysis*, **10**, 379 (1998).
8. A. I. Carim, S. M. Collins, J. M. Foley and S. Maldonado, *J. Am. Chem. Soc.*, **133**, 13292 (2011).
9. E. Fahrenkrug and S. Maldonado, *Acc. Chem. Res.*, **48**, 1881 (2015).
10. J. Gu, S. M. Collins, A. I. Carim, X. Hao, B. M. Bartlett and S. Maldonado, *Nano Lett.*, **12**, 4617 (2012).
11. R. N. Lyon, D. L. Katz, S. United and U. S. A. E. Commission, *Liquid-metals handbook*, U.S. G.P.O., Washington, D.C. (1954).
12. P. H. Keck and J. Broder, *Phys. Rev.*, **90**, 521 (1953).
13. C. Guminski, *J. Phase Equilib.*, **20**, 344 (1999).
14. C. Gumiński, *J. Mater. Sci.*, **24**, 2661 (1989).
15. I. Moschen, K. Schweizer, C. A. Wagner, J. Geis-Gerstorfer and F. Lang, *J. Dent. Res.*, **80**, 1753 (2001).
16. C. B. Eaker and M. D. Dickey, *Appl. Phys. Rev.*, **3**, 031103 (2016).
17. Y. Lu, Q. Hu, Y. Lin, D. B. Pacardo, C. Wang, W. Sun, F. S. Ligler, M. D. Dickey and Z. Gu, *Nat. Commun.*, **6**, 10066 (2015).
18. J. Mauzeroll, E. A. Hueske and A. J. Bard, *Anal. Chem.*, **75**, 3880 (2003).
19. M. Yamaguchi, S. Matsunaga, M. Shibasaki, B. Michelet, C. Bour and V. Gandon, in *Encyclopedia of Reagents for Organic Synthesis*, John Wiley & Sons, Ltd (2001).
20. M. Li, C. Li, F. Wang and W. Zhang, *Intermetallics*, **14**, 826 (2006).
21. P. Anres, M. Gaune-Escard and J. P. Bros, *J. Alloys Compd.*, **234**, 264 (1996).
22. S. C. Eady, S. L. Peczonczyk, S. Maldonado and N. Lehnert, *Chem. Commun.*, **50**, 8065 (2014).
23. C. A. Morris, A. K. Friedman and L. A. Baker, *Analyst*, **135**, 2190 (2010).
24. D. G. Haywood, A. Saha-Shah, L. A. Baker and S. C. Jacobson, *Anal. Chem.*, **87**, 172 (2015).
25. J. T. H. Tsai, C.-M. Ho, F.-C. Wang and C.-T. Liang, *Appl. Phys. Lett.*, **95**, 251110 (2009).
26. R. C. Gough, A. M. Morishita, J. H. Dang, M. R. Moorefield, W. A. Shiroma and A. T. Ohta, *Micro and Nano Syst. Lett.*, **3**, 4 (2015).
27. J. Orozco, C. Fernández-Sánchez and C. Jiménez-Jorquera, *Sensors*, **10**, 475 (2010).
28. C. G. Zoski and M. Wijesinghe, *Isr. J. Chem.*, **50**, 347 (2010).
29. R. Feeney and S. P. Kounaves, *Electroanalysis*, **12**, 677 (2000).
30. M. Joost, S. Cora, S. Sander, V. Jan and S. Jurriaan, *J. Micromech. Microeng.*, **19**, 065012 (2009).
31. J. Xu and C. P. Wong, *J. Appl. Polym. Sci.*, **103**, 1523 (2007).
32. E. Fahrenkrug, J. Biehl and S. Maldonado, *Chem. Mater.*, **27**, 3389 (2015).

33. J. N. Butler and M. L. Meehan, *Trans. Faraday Soc.*, **62**, 3524 (1966).
34. V. R. Erdelyi and M. Green, *Nature*, **182**, 1592 (1958).